

Spectral Extraction of Distinctive Latent Variables for Multimodal Data *

Shira Yoffe[†], Amit Moscovich[‡], and Ariel Jaffe[§]

Abstract. Multimodal datasets consist of observations generated by multiple types of sensors. Most works to date focus on uncovering latent structures in the data that appear in all modalities. However, important aspects of the data may appear only in one modality due to the differences between the sensors. Uncovering modality-specific attributes may provide insights into the sources of the variability of the data. For example, certain clusters may appear in the analysis of genetic but not epigenetic markers. Another example is hyper-spectral satellite imaging, where various atmospheric and ground phenomena are detectable using different parts of the spectrum. In this paper, we address the problem of uncovering latent structures that are distinctive to a single modality. Our approach is based on computing a graph representation of datasets from two modalities and analyzing the differences between their connectivity patterns. We provide an asymptotic convergence analysis for our method that is based on a product manifold model. To evaluate the performance of our method, we test its ability to uncover latent structures in multiple types of artificial and real datasets.

Key words. Manifold learning, spectral graph theory, kernel methods, multimodal data analysis, differential variable

MSC codes. 62-07, 62M15, 58C40, 62H25, 68T10

1. Introduction. Combining sets of high-dimensional measurements from different sources has become a key task in various fields. To name but a few examples, recent technological developments have enabled the simultaneous acquisition of gene expression, proteomic data, and spatial information at a single-cell level [29, 38]. In neuroscience, recent studies analyze PET scans of specific proteins and fMRI scans to gain insight into the development of degenerative disease [40]. In single-particle cryogenic electron microscopy, multiple views of a single protein or other macro-molecule are combined to recover the shape of the molecule and its manifold of motions [3, 26, 28, 41, 52]. In these settings, often referred to as multi-modal, the same object (i.e., an individual cell in genetics or a patient in neuroscience) is observed by two or more sets of sensors, where each set may generate thousands of variables [5, 22, 46]. A common goal is to provide a low-dimensional representation for downstream analysis based on the observations from the different sensors.

For a single modality, the manifold assumption has been the basis of numerous methods for data analysis developed in recent decades. A key assumption in manifold learning is that the high-dimensional observations $x_1, \dots, x_n \in \mathbb{R}^\ell$ can be well-approximated by a smooth map with a small number of variables $\theta \in \mathbb{R}^d$,

$$(1.1) \quad \theta_i \xrightarrow{T} x_i.$$

*Submitted to the editors DATE.

Funding: AM is supported by ISF grant 1662/22 and NSF-BSF grant 2022778.

[†]Department of Statistics and Data Science, Hebrew University of Jerusalem (shira.yoffe@mail.huji.ac.il).

[‡]Department of Statistics and Operations Research, Tel Aviv University (mosco@tauex.tau.ac.il).

[§]Department of Statistics and Data Science, Hebrew University of Jerusalem (ariel.jaffe@mail.huji.ac.il).

The main challenge of non-linear dimensionality reduction is to compute a low-dimensional representation of x_i associated with the latent variables θ .

Consider the setting where two different sensors, A and B, are used to take (simultaneous) snapshots of some object, yielding a collection of pairs $(x_i^A, x_i^B) \in \mathbb{R}^{\ell_A} \times \mathbb{R}^{\ell_B}$ where each pair contains two measurement modalities. Again, we assume that each observation can be approximated by the result of a continuous mapping applied to a set of latent variables,

$$(1.2) \quad (\theta_i, \psi_i^A) \xrightarrow{T_A} x_i^A \quad (\theta_i, \psi_i^B) \xrightarrow{T_B} x_i^B.$$

The latent parameters θ represent degrees of freedom that both sensors A and B can measure. In contrast, the latent variables ψ^A represent degrees of freedom that only A can measure and B is invariant to. The opposite holds for ψ^B . For example, A and B might represent two different color channels of a digital camera. Both channels are sensitive to changes in brightness, but each one is blind to changes in color outside of their respective spectrum. We illustrate our setting with a toy example in Figure 1. It shows several images of a single digit from the MNIST dataset. The upper row corresponds to modality A, where the digits differ in terms of orientation and scale. The bottom row shows the corresponding observations from modality B that can sense the orientation but is blind to the scale of the digit. In this example, the shared latent variable θ is the orientation, and the latent variable ψ^A that is exclusive to A is the digit size.

The primary objective of this work is to extract latent variables that are only captured by one of the sensors. By extracting these variables, we can map different aspects of the measured object that correspond to each sensor’s distinct capabilities.

1.1. Related work. A common goal in multi-modal analysis is to identify correlated subspaces or shared latent variables among different modalities. Canonical Correlation Analysis (CCA) is a well-known method designed for this purpose, seeking linear combinations of features from each view to maximize their correlation [18]. In many applications, the relation between the shared latent variables and the observed data may be highly non-linear, which limits the applicability of standard CCA. This motivated kernel-based extensions to CCA developed in recent years, [2, 21].

Several manifold learning methods have been designed to extract shared latent variables in the multi-modal settings. For instance, Diethe et al. [10] proposed a method to derive jointly smooth functions on multiple observed manifolds which can be utilized to find a joint embedding. Eynard et al. [12] introduced a common eigenbasis by extending spectral and diffusion methods to multiple modalities through simultaneous diagonalization of Laplacian matrices. Lee et al. [23] developed a method to find a joint representation of datasets under the manifold assumption, which preserves the intra-manifold and inter-manifold structures. Yair and Talmon [47] used Diffusion Maps with a local CCA-based kernel to extract shared variables. Zhao et al. [51] developed a multi-view manifold learning with locality alignment (MVML-LA) framework, integrating locality alignment in the latent space learning process. The Alternating Diffusion (AD) approach was developed by Lederman and Talmon [22] to find shared variables while discarding sensor-specific variables. Lindenbaum et al. [25] suggested a new distance metric for Diffusion Maps on multi-view problems.

Contrary to the works described above, in our work, we address the challenge of extracting

sensor-specific variables. Several works developed methods to find separating directions in the data for various tasks, such as classification, feature selection, and more. Linear Discriminant Analysis (LDA) [13] is a classic approach for finding a linear combination that maximizes the separation of the data, often used for supervised classification. Song et al. [37] have extended LDA to address feature selection problems. Later, a regularized LDA approach for a feature selection filter method was introduced by Sharma et al. [31]. The FKT transform [14] was developed for extracting features that represent the difference between two classes. FKT was later extended to the non-linear kernel Fukunaga-Kuntz transform (K-FKT), which is suitable for multi-class problems [24]. The detection of features via differentiating subspaces is also addressed by manifold-learning-based methods. DiSC [39] applies a spectral approach for feature extraction, which finds groups of features that differentiate between conditions. Cohen et al. [8] proposed a method that combines Riemannian geometry and spectral analysis for feature selection. A manifold learning approach for the detection of the sensor-specific variable under the multi-view setting was proposed by Shnitzer et al. [33] as an extension of alternating diffusion [22]. Katz et al. [19] developed a method to obtain a geodesic path between the kernels of two modalities. The path is then used to compute a set of representations for the two modalities.

Outline and contribution. Our research aims to address the challenge of detecting sensor-specific latent variables. In Section 2, we present the problem setting and review the relevant background in manifold learning and graph signal processing. In Section 3, we develop algorithms for extracting a single latent variable (Sec. 3.1) and multiple latent variables (Sec. 3.2). In Section 4 we analyze our approach under a product manifold setting [50] and derive guarantees for extracting a single variable. Evaluations based on simulated and real datasets are provided in Section 5.

2. Problem setting and related background. Consider two data sets $X^A \in \mathbb{R}^{n \times \ell_A}$ and $X^B \in \mathbb{R}^{n \times \ell_B}$, where the rows of both matrices consist of paired observations from two different sensors or modalities that satisfy the double manifold assumption of (1.2). The columns of X^A and X^B contain the features measured by the sensors A and B, respectively. Our aim is to compute a low-dimensional representation that is associated with the distinctive (or differential) latent parameters ψ^A and ψ^B . Our approach is graph-based. First, we build an undirected weighted graph for each modality,

$$(2.1) \quad G^A = (V, E^A, W^A), \quad G^B = (V, E^B, W^B).$$

The vertices $V = x_1, \dots, x_n$ correspond to the n observations and are the same in both graphs. The weights $W^A, W^B \in \mathbb{R}^{n \times n}$ are computed separately by two kernel functions,

$$(2.2) \quad K^A : \mathbb{R}^{\ell_A} \times \mathbb{R}^{\ell_A} \rightarrow \mathbb{R}, \quad K^B : \mathbb{R}^{\ell_B} \times \mathbb{R}^{\ell_B} \rightarrow \mathbb{R}.$$

A standard choice for the kernel is the Gaussian kernel using the Euclidean norm,¹

$$(2.3) \quad W_{i,j}^A = \exp(-\|x_i^A - x_j^A\|^2 / 2\sigma_A^2), \quad W_{i,j}^B = \exp(-\|x_i^B - x_j^B\|^2 / 2\sigma_B^2).$$

¹If one scales these weights by $2/((2\pi)^{d/2}\sigma^{d+2})$ then the eigenvalues of the random-walk and symmetric-normalized Laplacian matrices converge to the eigenvalues of the Laplace-Beltrami operator under the uniform density assumption. See Eq. (5) of Cheng and Wu [6]. In this paper, we mostly care about the eigenvector convergence so this scaling is not necessary.

Name	Description	Eq. ref
n	Number of observations	
x_i^A	i -th observation in dataset A	
θ	Shared variable	
ψ^A, ψ^B	Distinctive/differential variables of modalities A and B	
W^A, W^B	Weight matrices of each graph,	Eq. (2.3)
P^A, P^B	The symmetric operators	Eq. (2.4)
L^A, L^B	The symmetric Laplacian matrices	Eq. (2.5)
v^A, v^B	Eigenvectors of L^A, L^B	
λ^A, λ^B	Eigenvalues of L^A, L^B	
$H(L^A), H(L^B)$	Graph filters	Eq. (3.1)
\tilde{P}^A, \tilde{P}^B	The filtered operators	Eq. (3.2)
δ^A, δ^B	Differential vectors	Sec. 3.1
Δ_i^A, Δ_i^B	Differential vectors obtained by iterative process	Sec. 3.2
p	Uniform sampling density over the manifold \mathcal{M}	
f^A, f^B	Eigenfunctions of the LB operators of $\mathcal{M}^A, \mathcal{M}^B$	
η^A, η^B	Eigenvalues of the LB operators of $\mathcal{M}^A, \mathcal{M}^B$	
$\rho_X(f_k)$	The sampling operator, which evaluates f_k at a set of points X	
$\phi_k(X)$	Normalized vector of samples	Eq. (4.2)
$\ \cdot\ $	Matrix operator norm or Euclidean vector norm	
$\ \cdot\ _F$	Matrix Frobenius norm	

Table 1
Notation table

Common variations include replacing the fixed bandwidth σ with a density-dependent bandwidth [49], replacing the Euclidean norm with other norms or metrics such as the Mahalanobis distance or Wasserstein metric [20], and weights based on k -nearest-neighbor distances [6].

Let D^A, D^B be two diagonal matrices whose elements are equal to the degrees of the nodes in G^A, G^B , respectively, such that $D_{ii} = \sum_{j=1}^n W_{ij}$. We denote by P^A, P^B the operators,

$$(2.4) \quad P^A = (D^A)^{-0.5} W^A (D^A)^{-0.5}, \quad P^B = (D^B)^{-0.5} W^B (D^B)^{-0.5},$$

and the symmetric normalized Laplacian matrices by,

$$(2.5) \quad L^A = I - P^A, \quad L^B = I - P^B.$$

The operator P^A has the same eigenvectors as L^A , with eigenvalues equal to one minus the eigenvalues of L^A . The key idea in this paper is that degrees of freedom that correspond to the differential latent variables ψ^A, ψ^B can be extracted by analyzing differences in the

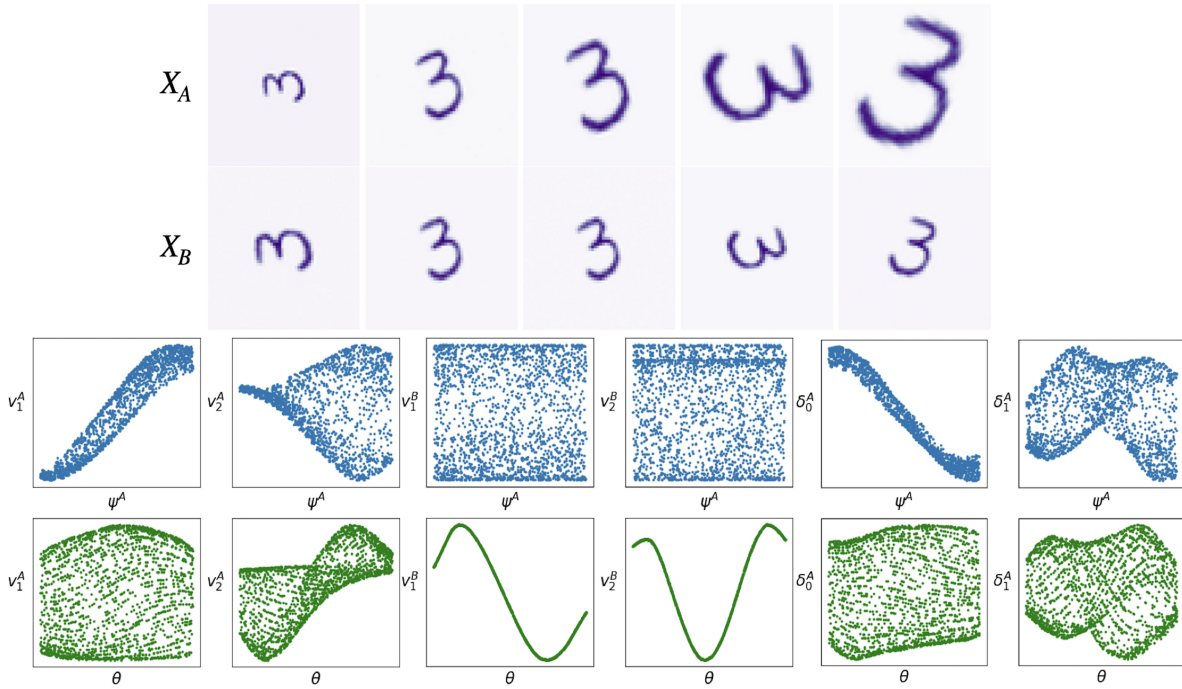


Figure 1. *Top row:* several examples of modality A: a single MNIST digit with varying size and orientation. *Second row:* the corresponding examples from modality B where the digits only vary in terms of orientation. *Bottom two rows:* Left four panels show the two leading Laplacian eigenvectors of P^A as a function of the orientation θ and size ψ^A . The middle four panels show the leading two eigenvectors of P^B as a function of θ, ψ^A . The four panels on the right show the two leading differential vectors (δ^A).

connectivity patterns of G^A and G^B . More specifically, we extract these differential degrees of freedom by analyzing the two graph Laplacians L^A and L^B , leveraging tools from the realm of graph signal processing.

2.1. Graph signal processing and graph filters. Let us first describe some notations and definitions. The signals that we consider are real functions $s : V \rightarrow \mathbb{R}$ defined on the vertices of the graph. Since the graph has n vertices we will identify them with vectors $s \in \mathbb{R}^n$. The symmetric normalized Laplacian matrix defined in Eq. (2.5) is positive semi-definite with at least one zero eigenvalue [34, 42]. We denote the eigenvalues in increasing order by $\lambda_0 = 0 \leq \lambda_1 \leq \dots \leq \lambda_n$ with corresponding eigenvectors $\{v_i\}_{i=0,1,\dots,n-1}$ that form an orthonormal basis of \mathbb{R}^n . The Laplacian eigenvectors are discrete analogues of the Fourier basis [27, 30, 34]. In fact, both are the eigenfunctions of the heat diffusion operator on their respective domain. The Laplacian matrix can be used as a smoothness functional for graph signals (see [42]). For the symmetric normalized Laplacian we have,

$$(2.6) \quad s^T L s = \frac{1}{2} \sum_{i,j=1}^n W_{i,j} \left(\frac{s_i}{\sqrt{D_{i,i}}} - \frac{s_j}{\sqrt{D_{j,j}}} \right)^2.$$

Combining Eq. (2.6) with the Courant-Fischer Theorem shows that the eigenvectors with the smallest eigenvalues are orthonormal minimizers of the RHS ([17, Theorem 4.2.11]),

$$(2.7) \quad v_\ell = \min_{\substack{\|s\|_2=1; \\ s \perp \{v_0, \dots, v_{\ell-1}\}}} \frac{1}{2} \sum_{i,j=1}^n W_{i,j} \left(\frac{s_i}{\sqrt{D_{i,i}}} - \frac{s_j}{\sqrt{D_{j,j}}} \right)^2.$$

Eq. (2.7) implies that for an eigenvector with a small eigenvalue, the \sqrt{D} -normalized values of neighboring vertices are close. This is analogous to classic Fourier analysis, where eigenfunctions with low eigenvalues have low spatial frequencies. Continuing this analogy, one can define the *Graph Fourier Transform* \hat{s} of a function $s \in \mathbb{R}^n$, and its inverse counterpart, the *Graph Inverse Fourier Transform* by

$$(2.8) \quad \hat{s}_\ell = \langle v_\ell, s \rangle, \quad s = \sum_{\ell=0}^{n-1} \hat{s}_\ell v_\ell.$$

Equation (2.8) provides the spectral domain representation of graph signals. Thus, one can define *graph spectral filtering* by including eigenvalue-based weights,

$$(2.9) \quad H(s) = \sum_{\ell=0}^{n-1} \hat{s}_\ell h(\lambda_\ell) v_\ell.$$

For example, the low-pass filter $h(\lambda_\ell; \tau) = \mathbf{1}_{\lambda_\ell \leq \tau}$ removes the high-frequency components of a signal and thus acts as a smoothing filter. In the following section, we design graph high-pass filters to discover latent variables that differentiate between two datasets.

3. Algorithms. In this section, we present algorithms for extracting a single differentiating latent variable (Sec. 3.1) and multiple variables (Sec. 3.2).

3.1. Extracting a single differentiating latent variable. To illustrate our approach, we use a simple example where X^B contains n observations sampled uniformly from a rectangle, thus $(\theta, \psi^B) \in [0, a] \times [0, b]$ and the dataset X^A contains only the first coordinate $\theta \in [0, a]$. We first compute the operators P^A, P^B via Eq. (2.4), the symmetric Laplacian matrices, L^A, L^B by Eq. (2.5) and their leading eigenvalues and eigenvectors, denoted respectively by λ_i^A, v_i^A and λ_i^B, v_i^B . Fig. 2 shows the four leading eigenvectors of P^A and P^B for the rectangle example as a function of θ, ψ^B . Since X^A contains only θ , the eigenvectors of P^A are similar to $\cos(\pi k \theta / a)$ and have no correlation with ψ^B , as shown in the top row. The observations in X^B contain both θ and ψ^B . The bottom panel shows that the leading two eigenvectors depend almost entirely on θ , the third almost entirely on ψ^B , and the fourth is a function of both parameters. The same phenomenon can also be observed in the rotating figure example in Fig. 1. The leading eigenvectors of P^A depend on the orientation angle (θ) as well as with the size of the digit (ψ^A), while the leading eigenvectors of P^B (ψ^B) only depend on the orientation angle.

To identify the distinctive parameter ψ^B , we design a filter that attenuates directions strongly associated with θ , and apply it to P^B . In standard filtering, the filter is designed based on prior assumptions or knowledge about the bandwidth of a signal. For example, a

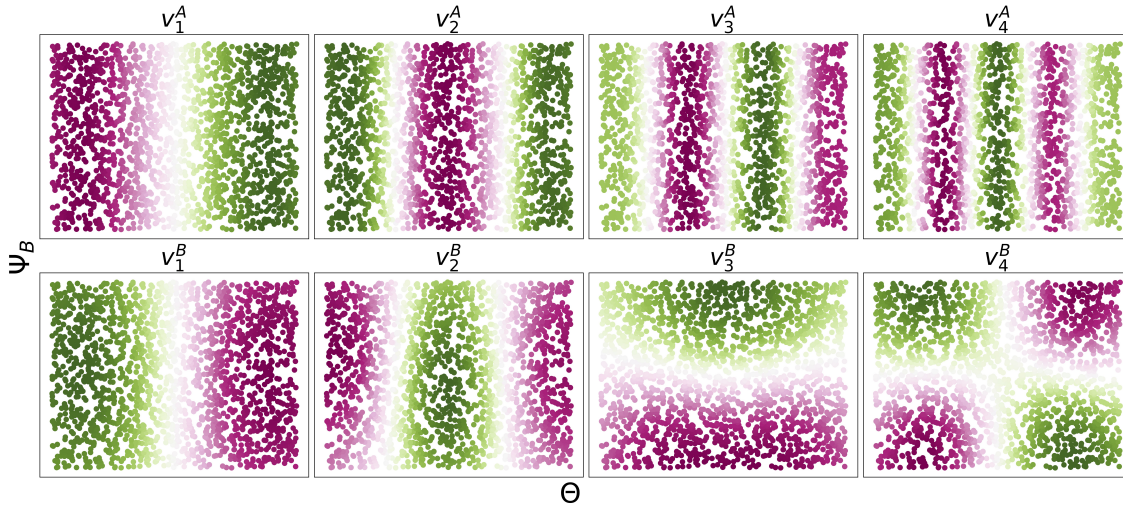


Figure 2. Line (X^A) vs. rectangle (X^B) example. The observation in X^B colored by the four leading eigenvectors of P^A (**top**) and the four leading eigenvectors of P^B (**bottom**). The shared variable θ is the x coordinate, and the differential variable ψ^B is the y coordinate.

graph low pass filter is based on an assumption that the signal is smooth with respect to the graph. Here, we design a **high-pass** filter function $H(L^A)$ based on the eigenvalues and eigenvectors of L^A . Let $h(\lambda) : [0, 1] \rightarrow [0, 1]$ denote a monotonically increasing function in λ . We define the graph filters $H(L^A)$ and $H(L^B)$ via,

$$(3.1) \quad H(L^A) = \sum_i h(\lambda_i^A) v_i^A (v_i^A)^T, \quad H(L^B) = \sum_i h(\lambda_i^B) v_i^B (v_i^B)^T.$$

Note that applying $H(L^A)$ to a vector y attenuates any component in y correlated with the leading eigenvectors of L^A . Our next step is to compute the following filtered operators by,

$$(3.2) \quad \tilde{P}^B = H(L^A) P^B H(L^A), \quad \tilde{P}^A = H(L^B) P^A H(L^B).$$

We refer to the leading eigenvectors of the filtered graphs, \tilde{P}^A and \tilde{P}^B , as *differential vectors* and denote them by δ^A and δ^B . In Sec. 4, we show that in contrast to the eigenvectors of the unfiltered operators P^A and P^B , under suitable assumptions, these vectors are associated only with modality-specific parameters ψ^A and ψ^B . For the two examples illustrated in Fig. 1 and Fig. 2, the filter $h(\lambda)$ was set to

$$(3.3) \quad h(\lambda_p) = \begin{cases} 1, & \text{if } \lambda_p > \tau. \\ 0, & \text{otherwise.} \end{cases}$$

For this filter, the matrix $H(L)$ becomes a projection matrix onto the subspace spanned by the eigenvectors in L^A that correspond to eigenvalues larger than τ . Fig. 3 shows the leading differentiating vectors of the filtered graph \tilde{P}^A and \tilde{P}^B . δ_0^B does not include information about θ , but is correlated with the second coordinate, ψ^B . All other differential vectors might

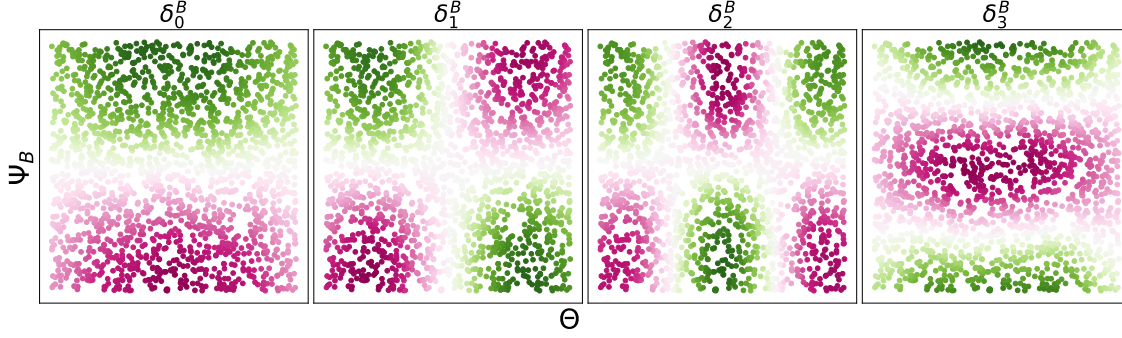


Figure 3. Line (X^A) vs. rectangle (X^B) example. The observation in X^B colored by the four leading eigenvectors of \tilde{P}^B . The shared variable θ is the x coordinate, and the differential variable ψ^B is the y coordinate.

still include some correlation with θ , but only as a cross-product with ψ^B (see, for example, δ_1^B and δ_2^B in Fig. 3). For the MNIST example, Fig 1 shows that δ^A is highly correlated with the differentiating parameter, which is the size. Alg. 3.1 summarizes the steps for extracting a single latent variable.

Algorithm 3.1 Recovering a single latent variable

Input: $X^A \in \mathbb{R}^{n \times \ell_A}$, $X^B \in \mathbb{R}^{n \times \ell_B}$ two matrices containing n samples with ℓ_A and ℓ_B features respectively. A filter function $h(\lambda) : [0, 1] \rightarrow [0, 1]$.

Output: Differential vectors $\delta^A, \delta^B \in \mathbb{R}^n$.

- 1: Compute the weight matrices W^A, W^B from X^A, X^B respectively using Eq. (2.3).
 - 2: Calculate the operators P^A, P^B using Eq. (2.4) and the symmetric normalized Laplacian matrices L^A, L^B using Eq. (2.5).
 - 3: Obtain the filtering matrices $H(L^A), H(L^B)$, via Eq. (3.1).
 - 4: Using Eq. (3.2), compute the filtered operators \tilde{P}^A, \tilde{P}^B .
 - 5: Compute the differential vector δ^A from the filtered operator \tilde{P}^A and δ^B from \tilde{P}^B .
-

3.2. Extracting multiple latent variables. In many applications, two datasets obtained with different sets of sensors may differ by multiple differentiating variables. In such cases, our only guarantee is that the leading differential vectors of each modality, δ_0^A and δ_0^B , are associated with differentiating variables; see our analysis in Sec. 4. There is, however, no similar guarantee regarding the next differential vectors, δ_1^A and δ_1^B . For example, δ_1^A may be equal to the cross product of two vectors associated with ψ_j^A and θ . Alternatively, it may be associated with the same differential parameter already discovered.

Let us provide a concrete example. In the example illustrated in Fig. 4, X^B contains n observations from a 3D cube, $\theta, \psi_1^B, \psi_2^B \in [0, a] \times [0, b] \times [0, c]$, where $a > b > c$. Similarly to the previous example, X^A contains only the first coordinate, the shared parameter $\theta \in [0, a]$. We aim to compute vectors associated with the distinctive parameters ψ_1^B, ψ_2^B . As known for the cube example, for $n \rightarrow \infty$, the first differential vector δ_0^B converges to $\cos(\pi\psi_1^B/b)$. Ideally, we would like the next differential vector to converge to $\cos(\pi\psi_2^B/c)$. However, it may also converge to $\cos(2\pi\psi_1^B/b)$ or to the product $\cos(\pi\theta/a) \cos(\pi\psi_1^B/b)$. The order of these vectors

Algorithm 3.2 Recovering multiple latent variables

Input: Matrices $X^A \in \mathbb{R}^{n \times \ell_A}$ and $X^B \in \mathbb{R}^{n \times \ell_B}$, containing n samples with ℓ_A and ℓ_B features respectively. K number of iterations. Filter function $h(\lambda) : [0, 1] \rightarrow [0, 1]$.

k_0 dimension of shared latent space.

Output: Differential vectors $\Delta_0^A, \dots, \Delta_K^A \in \mathbb{R}^n$.

- 1: Calculate the differential vector δ_0^A via Alg. 3.1 and output it as Δ_0^A .
- 2: Using Eq. (3.4), compute P^θ and its leading eigenvectors $V^{(0)} \in \mathbb{R}^{n \times k_0}$.
- 3: **for** $i \in \{1, \dots, K - 1\}$ **do**
- 4: Obtain $V^{(i)} \in \mathbb{R}^{n \times (k_0 + i)}$ by concatenating $V^{(i-1)}$ with the column vector Δ_{i-1}^A .
- 5: Compute Δ_i^A by applying Alg. 3.1 with inputs X^A and $V^{(i)}$ (substituting for X^B).
- 6: **end for**

is determined by their eigenvalues, which depend on the values of a, b , and c . Thus, an additional step is required to guarantee that: (i) the next differential vector is associated only with differential variables, and (ii) it is not redundant - it is associated with new variables that were not already discovered. To achieve this, we introduce an iterative method that adjusts the filters for P^A, P^B based on the vectors that were previously discovered. The main idea is to compute, at each iteration, new graphs for A and B . The weights of the new graphs are based only on the shared variables and the differential vectors computed in the previous iterations, and their eigenvectors are associated with the shared variables, the discovered differential variables, and all their cross-products. Thus, we can construct a new graph filter to attenuate all these eigenvectors. For simplicity, we present our approach for obtaining variables that are unique to X^A . A similar approach can be applied to obtain variables unique to X^B .

We denote the vectors obtained by our iterative process by Δ_i^A . The first vector Δ_0^A is equal to the differential vector δ_0^A . After computing Δ_0^A , we compute a representation that is associated only with the shared variables, denoted by $V^{(0)} \in \mathbb{R}^{n \times k_0}$, where k_0 is a parameter that is either provided as input or estimated from the data. To compute $V^{(0)}$, we propose a similar approach to [22], where the columns of $V^{(0)}$ are equal to the leading k_0 eigenvectors of the symmetric product of P^A and P^B ,

$$(3.4) \quad P^\theta = P^A P^B + P^B P^A.$$

The value of k_0 is typically estimated as the number of dominant eigenvalues in P^θ , such that the subset of eigenvectors, $V^{(0)}$, will span the space of the shared parameter θ . Our iterative process adds a single vector to the representation such that $V^{(1)} \in \mathbb{R}^{n \times (k_0 + 1)}$ is equal to the concatenation of $V^{(0)}$ with the differential vector Δ_0^A obtained by Alg. 3.1. Next, we compute a new differentiating vector Δ_1^A by applying Alg. 3.1 with $V^{(1)}$ as input. The algorithm computes a new filter that attenuates vectors associated with θ , the leading differentiating variables ψ_0 , and all their cross products. Thus, Δ_1^A is associated with a new differentiating variable. The steps for applying this approach are outlined in Algorithm 3.2. Initial results for the line vs. cube example are presented in the experiments section.

4. Analysis of the product manifold setting. In recent years, several works have derived convergence results, under the manifold setting, of the eigenvectors of the discrete Laplacian

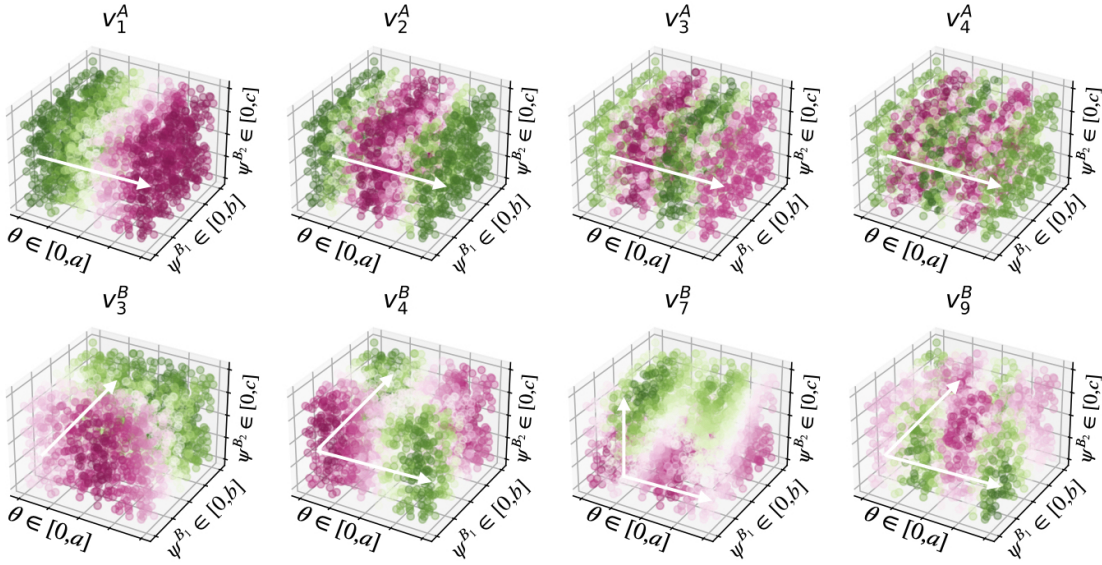


Figure 4. Line (X^A) vs. cube (X^B) example. The θ coordinate is shared between the two datasets. The second and third coordinates ψ_1^B, ψ_2^B are unique to X^B . **Top row:** The observations in X^B are colored by the leading eigenvectors of P^A . **Bottom row:** The observations in X^B colored by the leading eigenvectors of P^B . In both rows, the white arrow points to the direction of the dominant parameter.

to eigenfunctions of the Laplace Beltrami (LB) operator [4, 11, 15, 36, 43, 45]. For example, Cheng and Wu [7] derived an l_2 norm convergence result for the normalized and unnormalized Laplacian matrices, under the following assumptions:

- (i) The n observations are drawn independently according to a uniform distribution over a d -dimensional manifold \mathcal{M} .
- (ii) The smallest K eigenvalues of the Laplace-Beltrami (LB) operator over \mathcal{M} have single multiplicity, with a minimal spectral gap $\gamma_K > 0$.
- (iii) The graph weights are computed using a Gaussian kernel with a bandwidth parameter $\epsilon_n \rightarrow 0^+$ that satisfies $\epsilon_n^{d/2+2} > C_K \frac{\log n}{n}$ for some constant C_K .

Let dV denote the Riemannian volume form of \mathcal{M} and let the constant $p = 1/\int_{\mathcal{M}} dV$ denote the uniform sampling density. We denote by η_k the k^{th} smallest eigenvalue of the LB operator and by f_k a corresponding normalized eigenfunction, where

$$(4.1) \quad \int_{\mathcal{M}} f_k(x)^2 p dV(x) = 1.$$

We denote by $\rho_X(f_k) \in \mathbb{R}^n$ the sampling operator that evaluates the function f_k at a point set $X = \{x_1, \dots, x_n\} \subseteq \mathcal{M}$, and by $\phi_k(X) \in \mathbb{R}^n$ the vector of samples,

$$(4.2) \quad \phi_k(X) = \frac{1}{\sqrt{pn}} \rho_X(f_k).$$

In addition, we denote by $v_k \in \mathbb{R}^n$ the eigenvector of the symmetric-normalized graph Laplacian that corresponds to the k -th smallest eigenvalue. Similarly, we denote by $v_k^{(rw)}$ the

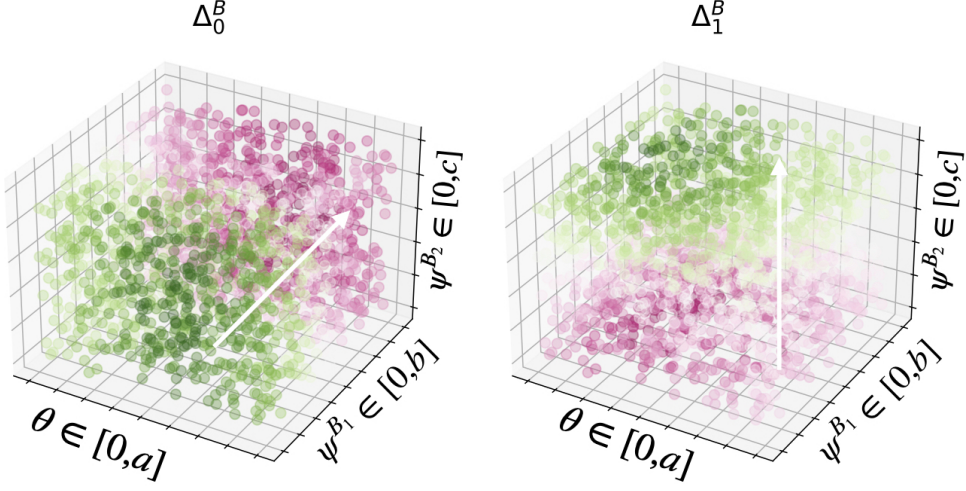


Figure 5. Line (X^A) vs. cube (X^B) example. The observations in X^B colored by the leading differential vectors of X^B obtained by algorithm 3.2. The white arrow points to the direction of the dominant parameter.

eigenvectors of the random walk Laplacian $L^{(rw)} = I - D^{-1}W$. The following convergence guarantee for $v_k^{(rw)}$ was proved by Cheng and Wu:

Theorem 4.1 (Theorem 5.5, [7]). *For $n \rightarrow \infty$ and under assumptions (i)-(iii), w.p. $> 1 - 4K^2n^{-10} - (4K + 6)n^{-9}$, the k^{th} eigenvector of the random-walk Laplacian satisfies*

$$(4.3) \quad \|v_k^{(rw)} - \alpha\phi(X)_k\|_2 = \mathcal{O}\left(\epsilon_n + \epsilon_n^{-d/4+1/2}\sqrt{\log n/n}\right), \quad \forall k \leq K,$$

where $v_k^{(rw)}$ is D -normalized such that $(v_k^{(rw)})^T D v_k^{(rw)} / (np) = 1$, ϵ_n is the bandwidth parameter used for the Gaussian affinity, equal to $\sigma^2/2$ in our notation (2.3), and $|\alpha| = 1 + o_p(1)$.

For our analysis, the convergence rate of α must be made explicit. Lemma Lemma A.1 in the archive shows that $|\alpha| - 1$ converges to zero at the same rate as in Eq. (4.3). Based on this theorem and a concentration result for the degree matrix, a similar concentration bound follows for the eigenvectors of the symmetric normalized Laplacian matrix:

Theorem 4.2. *For $n \rightarrow \infty$, under assumptions (i)-(iii), w.p. $> 1 - 4K^2n^{-10} - (4K + 8)n^{-9}$, the k^{th} eigenvector v_k of the symmetric-normalized Laplacian satisfies*

$$(4.4) \quad \|v_k - \alpha\phi_k(X)\|_2 = \mathcal{O}\left(\epsilon_n + \epsilon_n^{-d/4-1/2}\sqrt{\log n/n}\right), \quad \forall k \leq K,$$

where $\|v_k\| = 1$ is normalized and $|\alpha| = 1 + o_p(1)$.

The proof is in Section A.1.

Theorems 4.1 and 4.2 are concerned with the convergence of graph eigenvectors computed using a single dataset. However, in this paper, we are interested in the case of two datasets, where we assume that each was generated by random sampling on a product manifold. We start by providing the necessary notations and definitions for this case.

4.1. The product of manifold model. Let $\mathcal{M}_1, \mathcal{M}_2$ be two manifolds, and let $\mathcal{M} = \mathcal{M}_1 \times \mathcal{M}_2$ denote the product manifold, such that every point $x \in \mathcal{M}$ is associated with a pair of points $x_1 \in \mathcal{M}_1$ and $x_2 \in \mathcal{M}_2$. We denote by $\pi_1 : \mathcal{M} \rightarrow \mathcal{M}_1$ and $\pi_2 : \mathcal{M} \rightarrow \mathcal{M}_2$ the canonical projections of a point in \mathcal{M} to its corresponding points in $\mathcal{M}_1, \mathcal{M}_2$, respectively. Let $f_1 : \mathcal{M}_1 \rightarrow \mathbb{R}$ be a real function on the manifold \mathcal{M}_1 . The canonical projection operator can be used to define a function $f : \mathcal{M} \rightarrow \mathbb{R}$ known as the pullback of f_1 ,

$$(4.5) \quad f(x) = f_1(\pi_1(x)).$$

In this work we consider 3 disjoint sets of latent variables: ψ^A (latent variables unique to A), ψ^B (latent variables unique to B) and θ (common latent variables). Formally, we assume the existence of three latent manifolds $\mathcal{M}_1, \mathcal{M}_2, \mathcal{M}_3$ that are smooth transformations of the three sets of variables, ψ^A, ψ^B, θ , respectively. The two sets of observations X^A, X^B are sampled, respectively, from two product manifolds \mathcal{M}_A and \mathcal{M}_B , where

$$(4.6) \quad \mathcal{M}_A = \mathcal{M}_1 \times \mathcal{M}_3, \quad \mathcal{M}_B = \mathcal{M}_2 \times \mathcal{M}_3.$$

We assume that the observations in X^A and X^B are generated according to the following steps: (i) For each i , the latent variables $\theta_i, \psi_i^A, \psi_i^B$ are drawn independently. (ii) The observations x_i^A, x_i^B are computed according to

$$(4.7) \quad (\theta_i, \psi_i^A) \xrightarrow{T_A} x_i^A, \quad (\theta_i, \psi_i^B) \xrightarrow{T_B} x_i^B.$$

where T_A and T_B are smooth maps. We denote by $f_i^{(j)} : \mathcal{M}_j \rightarrow \mathbb{R}$ an i^{th} eigenfunction of the Laplace-Beltrami operator of the manifold \mathcal{M}_j . The eigenfunctions of the products $\mathcal{M}_A, \mathcal{M}_B$ are equal, up to a constant, to the pointwise product of the eigenfunctions of $\mathcal{M}_1, \mathcal{M}_2, \mathcal{M}_3$ (see Theorem 2 in [50], and discussion on warped product manifolds in [16]),

$$(4.8) \quad f_{l,k}^A(x) \sim f_l^{(1)}(\pi_1(x)) \cdot f_k^{(3)}(\pi_3(x)), \quad f_{m,k'}^B(x) \sim f_m^{(2)}(\pi_2(x)) \cdot f_{k'}^{(3)}(\pi_3(x)).$$

For the three manifolds $\{\mathcal{M}_j\}_{j=1}^3$, we denote by $\eta_i^{(j)}$ the i^{th} smallest eigenvalue, that corresponds to the eigenfunction $f_i^{(j)}$. We denote by $\eta_{l,k}^A, \eta_{l,k}^B$ the (l, k) -th smallest eigenvalue of the products $\mathcal{M}_A, \mathcal{M}_B$, as ordered by the following sums,

$$(4.9) \quad \eta_{l,k}^A = \eta_l^{(1)} + \eta_k^{(3)} \quad \eta_{m,k'}^B = \eta_m^{(2)} + \eta_{k'}^{(3)}.$$

The m^{th} smallest eigenvalue has the subscript (l, k) if $\eta_{l,k}^A$ is the m^{th} smallest eigenvalue of \mathcal{M}_A . We denote by $v_{l,k}^A, v_{m,k'}^B$ the eigenvectors of the symmetric normalized Laplacian matrices L^A, L^B . Similarly to the case of a single manifold, we denote by $\rho_X(f^A)$, the sampling operator that evaluates a function f^A at the points of X^A . In addition, we denote by $\rho_{\pi_i(X)}(f^{(i)})$ the sampling operator that takes a function $f^{(i)}$ on \mathcal{M}_i and evaluates it at the points $\pi_i(x_1), \dots, \pi_i(x_n)$. We denote by p_A, p_B the sampling density over the manifolds $\mathcal{M}_A, \mathcal{M}_B$. The following lemma, which forms the basis of our analysis, shows that the vectors $v_{l,k}^A$ and $v_{m,k'}^B$ are nearly orthogonal.

Lemma 4.3. *Let $\mathcal{M}_A = \mathcal{M}_1 \times \mathcal{M}_3$ and $\mathcal{M}_B = \mathcal{M}_2 \times \mathcal{M}_3$. Let $v_{l,k}^A, v_{m,k'}^B$ be, respectively, the (l, k) -th and (m, k') -th unit-length eigenvectors of the Laplacian matrices L^A, L^B . We assume that the corresponding eigenvalues $\eta_{l,k}^A$ and $\eta_{m,k'}^B$ are both within the K smallest eigenvalues of their respective spectra. Under assumptions (i)-(iii), as $n \rightarrow \infty$ the following holds with probability $> 1 - 12K^2n^{-10} - (8K + 16)n^{-9}$,*

$$(4.10) \quad |(v_{l,k}^A)^T v_{m,k'}^B| = \begin{cases} 1 - \mathcal{O}\left(\epsilon_n + \sqrt{\frac{\log n}{n\epsilon_n^{d/2+1}}}\right), & \text{if } k = k' \text{ and } l = m = 0. \\ \mathcal{O}\left(\epsilon_n + \sqrt{\frac{\log n}{n\epsilon_n^{d/2+1}}}\right), & \text{otherwise.} \end{cases}$$

Lemma 4.3 proves that the eigenvectors of the Laplacian matrices, excluding those that are associated only with the shared variable θ , are almost orthogonal. The lemma is the main building block for the proof of our convergence guarantee derived for Alg. 3.1. For simplicity, in our proof, we set the filter $H(L^A)$ to be a threshold function with parameter τ as defined in Eq. (3.3). Given a matrix V^A of size $n \times K_A$ whose columns consist of the eigenvectors of L^A with eigenvalue smaller than τ , the filter matrix $H(L^A)$ is equal to the following projection matrix, which we denote by $Q^A = I - V^A(V^A)^T$. In addition, for the analysis we make one modification to Alg. 3.1. In step 4 of the algorithm, we apply a low pass filter to P^B and attain P_τ^B given by

$$(4.11) \quad P_\tau^B = \sum_{l,k;\lambda_{lk}^B \leq \tau} (1 - \lambda_{l,k}^B) v_{l,k}^B (v_{l,k}^B)^T.$$

Thus, the operator computed in step 4 of the algorithm is equal to $\tilde{P}_A = Q^A P_\tau^B Q^A$. We denote by K_B the number of eigenvectors in L_B whose eigenvalue is smaller than τ , and by $K = \max(K_A, K_B)$. Let $\eta_{1,0}^B$ be the first eigenvalue whose corresponding eigenfunction is associated with a differential variable. We assume that the chosen threshold is sufficiently large such that $\tau > \eta_{1,0}^B$. The following theorem gives the convergence rate of the leading differential vector δ^B to the eigenfunction $f_1^{(2)}$ of \mathcal{M}_2 .

Theorem 4.4. *Let X^A, X^B be two sets of n points sampled uniformly at random from the product manifold $\mathcal{M}_A = \mathcal{M}_1 \times \mathcal{M}_3, \mathcal{M}_B = \mathcal{M}_2 \times \mathcal{M}_3$ respectively. Let*

$$(4.12) \quad \delta^B = \arg \max_{\|v\|=1} v^T Q^A P_\tau^B Q^A v$$

be the differential vector obtained in step 5 of Alg. 3.1. For $n \rightarrow \infty$ and assuming (i)-(iii) hold for both manifolds, the following holds with probability $1 - 4K^2n^{-10} - (2K + 6)n^{-9}$,

$$(4.13) \quad \left\| \delta^B - \frac{\alpha}{\sqrt{pn}} \rho_{\pi_2(X)} f_1^{(2)} \right\|^2 \leq \mathcal{O}(K\epsilon_n) + \mathcal{O}\left(K \sqrt{\frac{\log n}{n\epsilon_n^{d/2+1}}}\right).$$

Theorem 4.4 implies that given a sufficient number of samples, the leading vector δ^B of the filtered operator \tilde{P}^B computed in step 5 of Alg. 3.1 converges to the leading eigenfunction of \mathcal{M}_2 . Thus, it captures the leading differential variable that is not shared between the two datasets. Note, however, that the bound is on the squared distance, which implies that the rate of convergence is slower than the rate in Theorem 4.2.

Proof sketch for Theorem 4.4. Recall that $\eta_{l,k}^A = \eta_l^{(1)} + \eta_k^{(3)}$ denotes the eigenvalues of the Laplace-Beltrami operator on the product manifold $\mathcal{M}_A = \mathcal{M}_1 \times \mathcal{M}_3$. The eigenvalues $\eta_{0,k}$ correspond to eigenfunctions $f_{0,k}$ that are functions of the shared variable θ only (see Eq. (4.8)). For the analysis, we partition the columns of V^A , which contain the eigenvectors of L^A with smallest eigenvalues, to two parts: (i) $V^{A\theta}$, which includes only the eigenvectors of the form $\{v_{0,k}\}$ which correspond to eigenfunctions $f_{0,k}$, and (ii) $V^{A\psi}$ which includes vectors $\{v_{l,k}\}$ where $l \neq 0$. In addition, we define the following projection matrices:

$$(4.14) \quad Q^{A\theta} = I - V^{A\theta}(V^{A\theta})^T, \quad Q^{A\psi} = I - V^{A\psi}(V^{A\psi})^T.$$

Note that due to the orthogonality of $V^{A\psi}$ and $V^{A\theta}$, we have

$$(4.15) \quad Q^{A\theta}Q^{A\psi} = I - V^A(V^A)^T.$$

Similarly, we denote by $V^{B\theta}$ a matrix that contains, as columns, the eigenvectors of L^B that correspond to $\lambda_{0,k'}^B$, and by $Q^{B\theta} = I - V^{B\theta}(V^{B\theta})^T$. We prove Theorem 4.4 in three steps:

Step 1: Let $E_1 = Q^{B\theta}P_\tau^BQ^{B\theta}$. The projection matrix $Q^{B\theta}$ is the *ideal filter* in the sense that it perfectly removes the leading eigenvectors that are functions of the shared variable.

We show that the leading eigenvector of E_1 converges, for large n , to $\rho_X(f_{1,0}^B)$.

Step 2: Let $E_2 = Q^{A\psi}Q^{A\theta}P_\tau^BQ^{A\theta}Q^{A\psi}$. This is the filtered operator \tilde{P}^B , computed in step 4 of Algorithm 3.1. We bound the spectral norm of the difference of E_1 and E_2 .

Step 3: Using the Davis-Kahan theorem, we bound the spectral norm of $E_1 - E_2$ and conclude that the leading eigenvector of E_2 converges to $\rho_X(f_{1,0}^B)$.

A detailed proof of each step appears in Section A.5 of the archive.

5. Simulations. We compare our algorithm to two baselines. The first is a linear CCA method, adapted to obtain the differentiating directions instead of the shared ones. Let V_{CCA} be a matrix that contains the vectors that span the shared subspace obtained by CCA. We project the data in X^B onto the subspace orthogonal to V_{CCA} and compute the leading eigenvector via,

$$(5.1) \quad v = \arg \max \|(I - V_{CCA}(V_{CCA})^T)Xv\|.$$

The second baseline is the Fukunaga-Koontz Transform ('FKT'). We apply the FKT over an unnormalized Laplacian graph, $L = D - W$, by computing the leading eigenvectors of the following operators:

$$(5.2) \quad \tilde{L}_{FKT}^B = (L^A + L^B)^{-1}L^B, \quad \tilde{L}_{FKT}^A = (L^A + L^B)^{-1}L^A.$$

We evaluated our method and the baselines on both simulated and real datasets. In both cases, we performed a total of twenty iterations with increasing Gaussian noise added to one of the datasets. For the evaluation criteria we used the following two scores:

- **Ground truth correlation:** We construct the ground truth vector of the target latent parameter (ψ_1, \dots, ψ_n) and compute its normalized correlation with the differential vector that each method outputs.

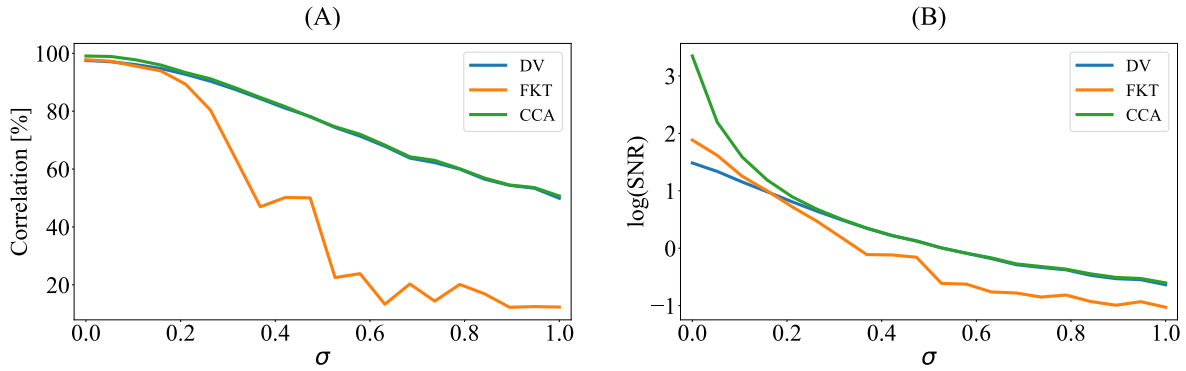


Figure 6. The line vs. rectangle example. (A) The correlation of $\cos(\psi^B \pi/b)$ for the Differential vectors (blue), the FKT eigenvectors (orange) and the adapted CCA singular vectors (green), as a function of the noise level σ . (B) The log signal-to-noise ratio (SNR) of the three methods as a function of σ .

- **Signal to noise ratio (SNR):** First, we order the coordinates of the differential vector according to their corresponding true latent parameter value. Denoting this reordered differential vector by $\tilde{\delta}_i$, we take the difference between $\tilde{\delta}_i$ and a sliding-window smoothed version of it $s_l = \sum_{i=l-k}^l \tilde{\delta}_i / (k+1)$. The sliding-window standard deviation is $n_l = \sqrt{\sum_{i=l-k}^l (\tilde{\delta}_i - s_l)^2 / k}$. Finally we compute $\text{SNR} := \sum_l (s_l)^2 / \sum_l (n_l)^2$. The advantage of the SNR evaluation metric compared to the ground truth correlation is that it does not require precise knowledge of the Laplacian eigenfunction that corresponds to the latent parameter. The code for some of the examples in this paper is available online at <https://github.com/ShiraAlon/Spectral-Extraction-of-Distinctive-Latent-Variables-for-Multimodal-Data>. ■

5.1. Rectangle vs. Line. Here, we present results of the line vs. rectangle experiment described in Sec. 3.1. The two panels in Figure 6 shows the outcome of the two evaluation metrics. The left panel shows the correlation between the outcome of the three methods and the theoretical differential vector. The correlation of all three methods is quite similar for low noise levels σ . As the noise levels increase, the FKT method experiences a faster decline in accuracy compared to our approach. In this example, the differential variable is a linear function of the input, which makes CCA a suitable approach. Our approach, however, obtained similar results even in this case. When examining the signal-to-noise ratio (right panel), we observe that their values are relatively close for all three methods. Notably, the FKT method exhibits the lowest SNR. At low levels of σ , the CCA’s SNR measure is higher than our method. However, as σ increases, the SNR of both methods converges.

5.2. Circle vs. Torus. The dataset $X^A \in \mathbb{R}^{N \times 2}$ contains $n = 2000$ points randomly drawn on the circle $(R \cos(\theta), R \sin(\theta))$, with a fixed radius R and $\theta \sim U[0, 2\pi]$. The dataset $X^B \in \mathbb{R}^{N \times 3}$ contains points sampled from a 3-dimensional torus,

$$(5.3) \quad ((R + r \cos(\psi^B)) \cos(\theta), (R + r \cos(\psi^B)) \sin(\theta), r \sin(\psi^B))$$

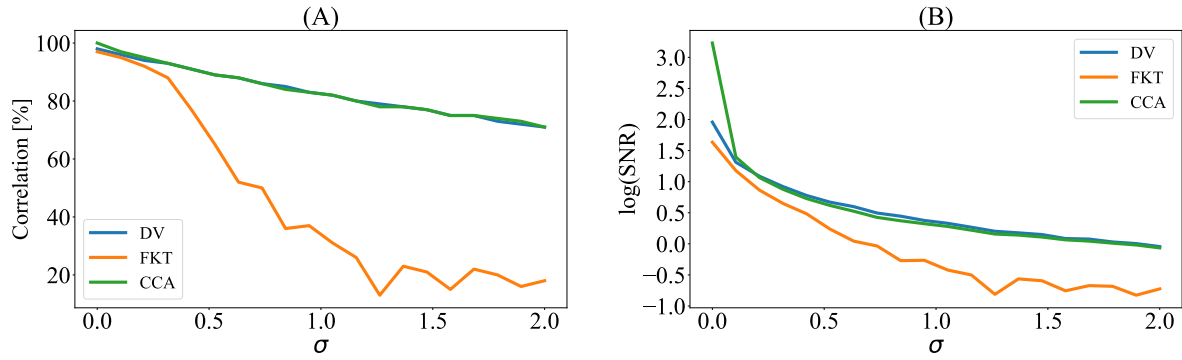


Figure 7. The circle vs. torus examples. (A) The cross-correlation between $\cos(\psi^B)$ and the leading differential vector computed by all methods, as a function of the noise level σ . (B) The SNR metric of the three methods as a function of σ .

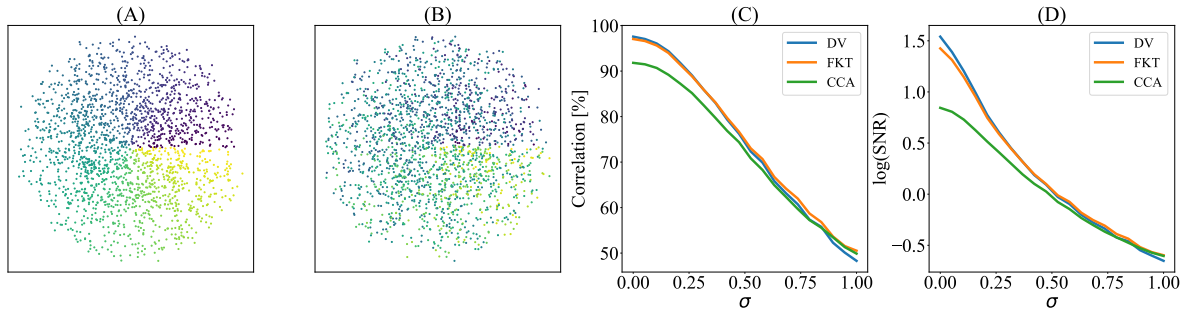


Figure 8. (A) Observations generated from the area of a circle $x_i = (r_i \cdot \cos(\psi_i^A), r_i \cdot \sin(\psi_i^A))$, colored by the parameter ψ_i^A . (B) The rotated data, $(r_i \cdot \cos(\psi_i^B), r_i \cdot \sin(\psi_i^B))$ colored by ψ_i^A . (C) The correlation of the leading Differential vector computed by three methods with $\cos(\psi^B)$, as a function of σ . (D) The log SNR of the different methods as a function of σ .

where θ is the same angle used in the corresponding point in X^A , and $\psi^B \sim U[0, 2\pi]$. As observed in Fig. 7, the ground truth correlation score achieved by our method closely resembles that of the CCA and both outperform the FKT method, especially for high noise levels. The SNR of our method and the CCA are very close and higher than the SNR of the FKT method for all noise levels.

5.3. Rotation around the axis. Here, we used an example from Coifman, Marshall & Steinerberger [9]. The first dataset $X^A \in \mathbb{R}^{N \times 2}$ comprises of $n = 2000$ randomly generated samples from a disk $(r \cdot \cos(\psi^A), r \cdot \sin(\psi^A))$, where $r \sim U[0, R]$ and $\psi^A \sim U[0, 2\pi]$ are drawn independently. The observations of X^B are $(r \cdot \cos(\psi^B), r \cdot \sin(\psi^B))$ where r is the same radius of the corresponding observation in X^A but the angle ψ^B is drawn anew. As shown in Fig. 8, both our algorithm and the FKT method achieved similar results for every value of σ . The accuracy of CCA is lower for low noise levels and decreases to similar levels with σ .

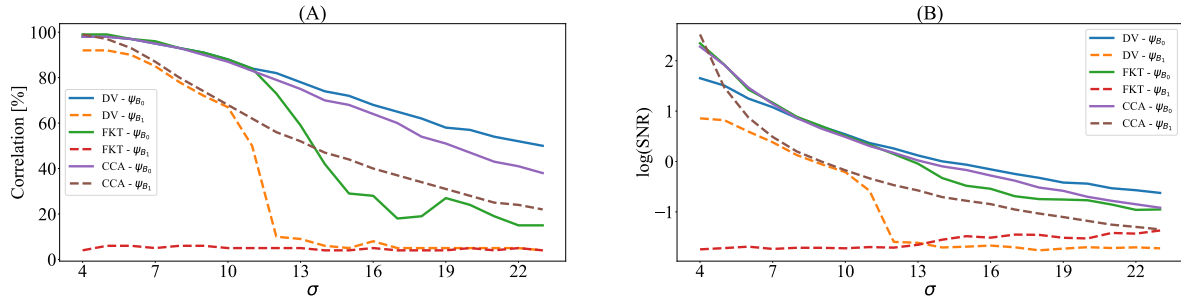


Figure 9. *The line vs. 3D cube example. (A) The three solid lines show the correlation of the leading differential vectors, as computed by the three methods, with $\cos(\pi\psi^B/b)$. The dashed lines show the correlation of the second differential vectors with $\cos(\pi\psi_2^B/c)$. (B) The SNR metric of the same three methods.*

5.4. Line vs. Cube. This is the example in Fig. 9 described in Sec. 3.2. To account for the multiple differentiating parameters, we use an iterative approach. To ensure a meaningful comparison between our approach to the CCA and FKT methods, we followed a similar iterative procedure: Upon identifying a vector correlated with the first differentiating parameter, we concatenated it with the vector of the shared parameter between the two datasets. Next, we projected the second dataset onto its complementary space via $(I - P(\theta, \psi_1^B))X^B$ and computed the leading singular vector. As shown in Fig. 9, the accuracy of the second vector deteriorates faster than the first for all methods. The accuracy in detecting ψ_1^B by the FKT approach is also high for low levels of σ but decreases more significantly than our method.

5.5. Stochastic Block model: four vs. five communities. We generated two random graphs with $n = 800$ nodes according to the stochastic block model [1]. In this model, every edge is a Bernoulli random variable, and the nodes are partitioned into communities (or blocks). The variable p represents the probability of an edge connecting two nodes within the same community, while the variable q represents the probability of an edge connecting two nodes from different communities. The first graph, denoted G_A , includes four communities with 200 nodes each, whereas, in the second graph, denoted G_B , the first community was split into two smaller communities of 100 nodes each, see Fig. 10. The goal is to correctly cluster the first 200 nodes of graph G_B , which in G_A belongs to one community. We repeated the experiment twenty times with $p = 0.33$ and increasing values for the q parameter starting with $q = 0.05$. Note that separating the nodes correctly becomes significantly more challenging when $q \rightarrow p$. As displayed in Fig. 10, for $q \leq 0.5p$, our approach achieves more than 95% accuracy. The performance rapidly deteriorates for $q > 0.5p$. For our approach, the most relevant eigenvector was always the leading one. In contrast, to obtain reasonable results for FKT and CCA we had to search deeper in the spectrum. In Fig. 10 we show their result using the fourth vector. In particular, the FKT algorithm performs badly even for low values of q . The CCA obtains similar but slightly worse results than our approach.

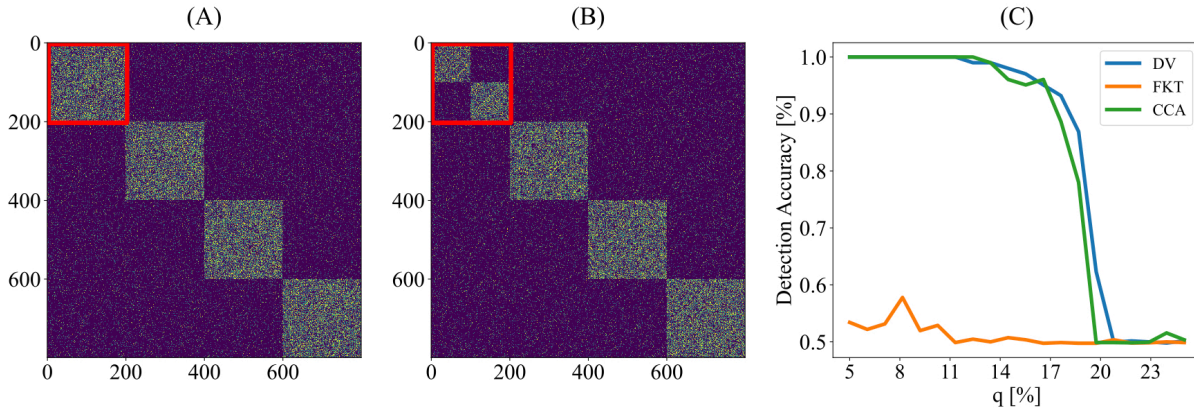


Figure 10. (A) Stochastic Block model with four communities. (B) A stochastic Block model with five communities, where the first community in X^A was divided into two. (C) The accuracy of separating the first two communities.

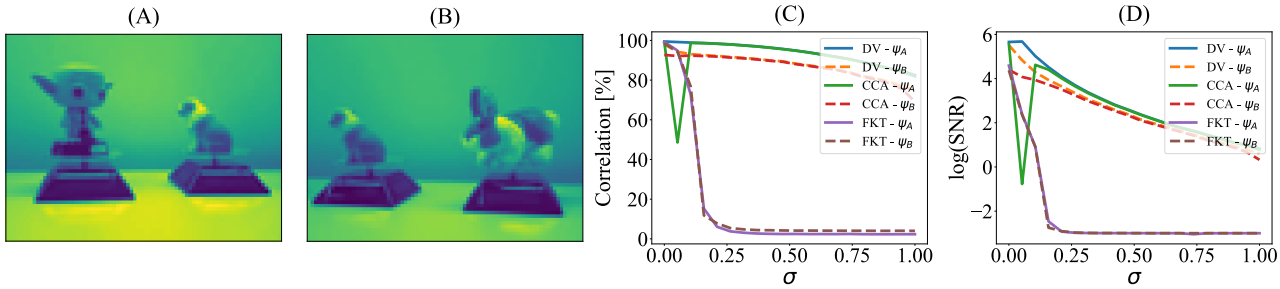


Figure 11. (A) A single image from dataset X^A that shows the Yoda figure on the left and the dog figure on the right. (B) A single image from X^B shows the same dog figure as in X^A on the left and the rabbit figure on the right. (C) The solid lines show the correlation of the leading differential vectors of X^A with the ground truth vector computed by slicing the images of X^A . The dashed line shows similar metrics for the leading differential vectors of X^B . (D) The log SNR metric.

5.6. Two videos with different objects. Datasets X^A, X^B are videos containing 4050 images of rotating figures, created by [22]². Each video includes two rotating figures, Yoda and Bulldog in X^A and Bunny and Bulldog in X^B . The rotation angle of the Yoda, Bunny, and the Bulldog are the hidden variables, ψ^A, ψ^B , and θ , respectively. We aim to extract the differentiating variables, ψ^A , and ψ^B . To obtain the "true" rotation angle of each figure, we split the images in half, with each one including only one doll. Based on these halves, we construct Laplacian graphs and treat their leading eigenvectors as the ground truth for the rotation angles, ψ^A, ψ^B , and θ . As seen in Fig. 11, our approach, as well as the FKT method, have high accuracy for low σ . However, the FKT accuracy decays quickly when the noise increases while the accuracy of our method remains high.

²This dataset is available online at <https://roy.lederman.name/alternating-diffusion/>

5.7. Textual description of birds. We employ captions from the Caltech-UCSD Birds (CUB) dataset [44] for an example of a multi-view problem [32]. This dataset contains 11,788 photographs of birds within their natural habitats. Each image is accompanied by ten detailed captions depicting the visual attributes and characteristics of the bird, collected through the Amazon Mechanical Turk (AMT) platform. In our analysis, we used two different captions related to 470 images from eight different bird types as X^A and X^B . To further distinguish between the two datasets, we excluded all the colors' names from the captions of the second writer, effectively assuming that this writer is "color-blind". The vectorization of the text was done after removing stop-words and stemming via the Bag-of-words method with N-grams ranging from 1 to 5. Then, using PCA, we reduced both dataset dimensions to $d = 5$.

As seen in Fig. 12, we deliberately selected two bird types, the *Cerulean Warbler* and the *Yellow Warbler*, due to their striking resemblance in all aspects except color. When color descriptions are omitted, these two bird types exhibit significant similarity and could be easily confused as the same species. This issue can be likened to the problem described in the Stochastic Block model example. In this context, the differentiating parameter of the two datasets is the number of distinct communities (types), and our goal is to cluster these birds correctly. Applying our approach, we were able to separate these birds into the two different types correctly, as demonstrated in Fig. 12.

5.8. Depth images. The NYU-Depth V2 dataset contains images of indoor scenes taken by both a regular camera and a depth camera from the Microsoft Kinect [35]. We focused on one scene, treating the RGB photo as one modality and the depth photo as the second modality. As Fig. 13 shows, both images include the main elements of the scene. While the RGB photo captures all the details of different objects that are in the scene, the depth camera captures only the shape of the voluminous objects.

Here, X^A consists of flattened $8 \times 8 \times 3$ patches of the RGB photo, and X^B consists of flattened 8×8 patches of the depth photo. Thus, the kernel matrices reflect the correlation between the different patches in the image, regardless of their position. We aim to extract all the details that are included in X^A , but are missing by X^B . It can be seen in Fig. 13 that the leading differential vectors of modality A do include the segmentation of all the small objects in the scene, whereas the differentiating vectors of modality B display the general depth of the space and show almost no details.

Appendix A. Proofs.

A.1. Proof of Theorem 4.2: eigenvector convergence rate for the symmetric normalized Laplacian.

Proof. The eigenvectors of the symmetric-normalized Laplacian satisfy $v_k \propto D^{1/2}v_k^{(rw)}$, where D is the diagonal matrix of degrees [42, Prop 3.(2)]. We may freely choose a multiplicative constant for eigenvectors, so we take $v_k^{(rw)}$ D -normalized such that $(v_k^{(rw)})^T D v_k^{(rw)} = pn$ as in Theorem 5.5, [7] and $v_k = \frac{D^{1/2}}{\sqrt{pn}}v_k^{(rw)}$ so that $\|v_k\|^2 = \frac{(v_k^{(rw)})^T D v_k^{(rw)}}{pn} = 1$. By the triangle

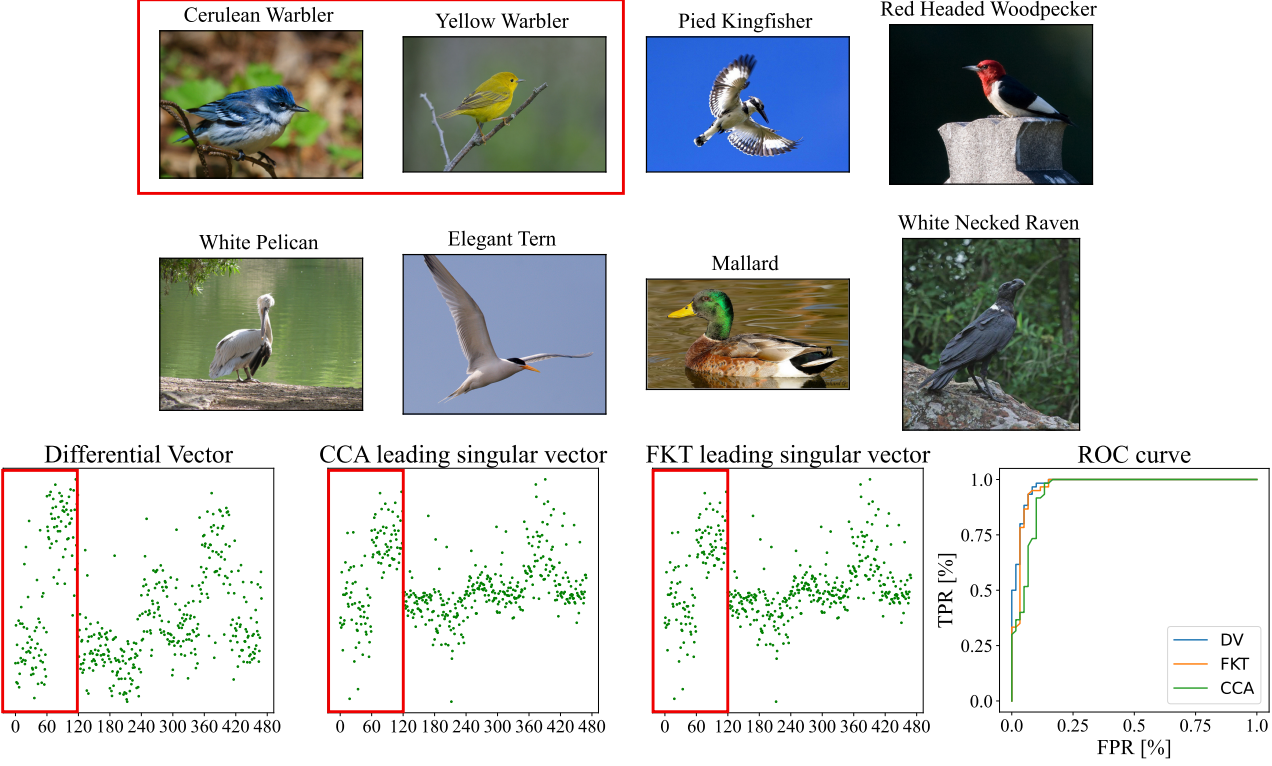


Figure 12. *Top panel: The eight distinct bird types, each has approximately 60 different photographs. Notably, the Cerulean Warbler and the Yellow Warbler, highlighted in red, bear a close resemblance to each other, primarily distinguished by color while being similar in all other aspects. Bottom left: The differential vector, yield by filtering P^A . The red Marking corresponds to entries associated with observations of the two similar bird types previously mentioned. Bottom right: ROC curve for the separation of the two bird types.*

inequality,

$$(A.1) \quad \left\| v_k - \alpha \phi_k(X) \right\| = \left\| \frac{D^{1/2}}{\sqrt{pn}} v_k^{(rw)} - \alpha \phi_k(X) \right\|$$

$$(A.2) \quad = \left\| \frac{D^{1/2}}{\sqrt{pn}} v_k^{(rw)} - v_k^{(rw)} + v_k^{(rw)} - \alpha \phi_k(X) \right\|$$

$$(A.3) \quad \leq \left\| \frac{D^{1/2}}{\sqrt{pn}} v_k^{(rw)} - v_k^{(rw)} \right\| + \|v_k^{(rw)} - \alpha \phi_k(X)\|.$$

By 4.1 [7, Theorem 5.5], the second term is bounded w.p. $> 1 - 4K^2 n^{-10} - (4K + 6)n^{-9}$ as

$$(A.4) \quad \|v_k^{(rw)} - \alpha \phi_k(X)\| = \mathcal{O} \left(\epsilon_n + \epsilon_n^{-d/4-1/2} \sqrt{\log n/n} \right).$$

To bound the first term, we require an additional concentration bound on the degree matrix. By [7, Lemma 3.5], for large values of n , with probability $> 1 - 2n^{-9}$, the following holds

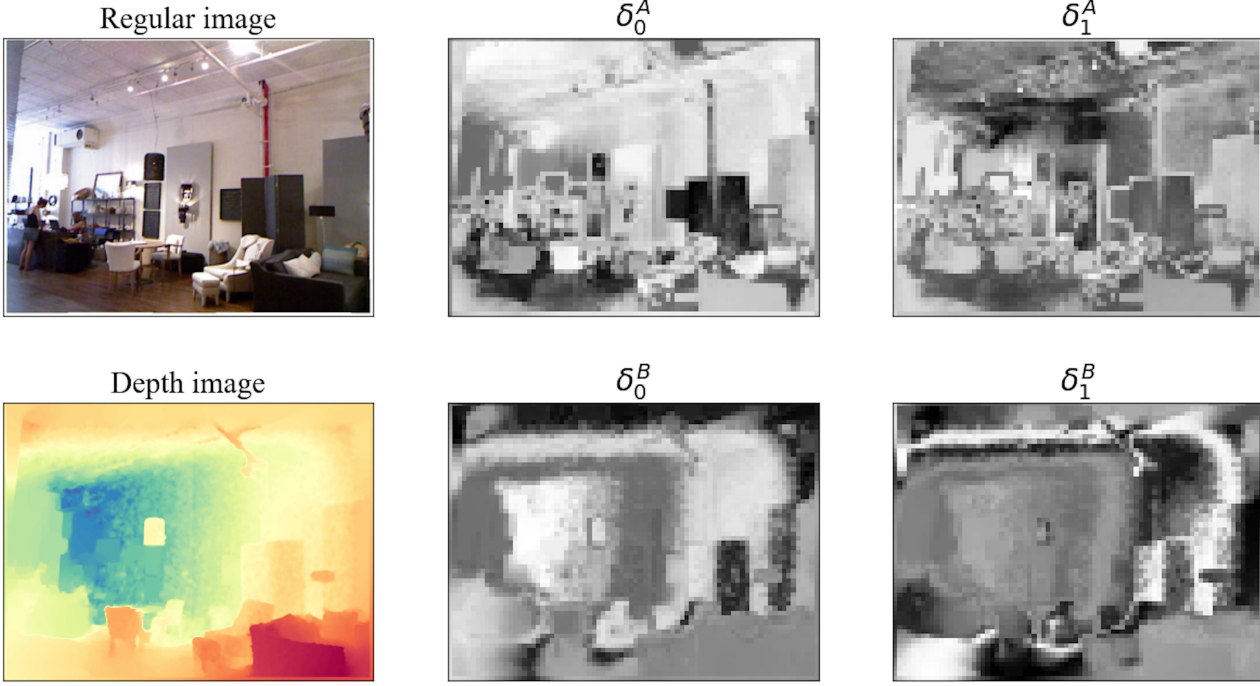


Figure 13. Left column: image taken by a regular camera (top) and by the depth camera (bottom) Middle and right columns: Two leading differential vectors of \hat{P}^A (top) and of \hat{P}^B (bottom).

uniformly for all i :

$$(A.5) \quad D_{ii}/n = m_0 p + \mathcal{O}\left(\epsilon_n + \epsilon_n^{-d/4} \sqrt{\log n/n}\right).$$

Where m_0 is a kernel-dependent constant and p is the uniform density on the manifold. For the Gaussian kernel $m_0 = 1$, so we can simply write

$$(A.6) \quad D_{ii}/pn = 1 + \mathcal{O}\left(\epsilon_n + \epsilon_n^{-d/4} \sqrt{\log n/n}\right).$$

By taking the square root of both sides and substituting $\sqrt{1+x} = 1 + \mathcal{O}(x)$ for $x \rightarrow 0$, we obtain that the same rate of convergence holds for the square root

$$(A.7) \quad \sqrt{D_{ii}/pn} = 1 + \mathcal{O}\left(\epsilon_n + \epsilon_n^{-d/4} \sqrt{\log n/n}\right).$$

We now bound the first term of the right-hand side of Eq. (A.3),

$$(A.8) \quad \left\| \frac{D^{1/2}}{\sqrt{pn}} v_k^{(rw)} - v_k^{(rw)} \right\| = \left\| \left(\frac{D^{1/2}}{\sqrt{pn}} - I \right) v_k^{(rw)} \right\| \leq \left\| \left(\frac{D^{1/2}}{\sqrt{pn}} - I \right) \right\| \|v_k^{(rw)}\|,$$

where the first term in the RHS denotes the operator norm. The operator norm of a diagonal matrix is simply the maximum absolute value of the diagonal elements,

$$(A.9) \quad \left\| \left(\frac{D^{1/2}}{\sqrt{pn}} - I \right) \right\| = \max_i \left| \frac{D_{ii}^{1/2}}{\sqrt{pn}} - 1 \right| = \mathcal{O}\left(\epsilon_n + \epsilon_n^{-d/4} \sqrt{\log n/n}\right).$$

where this bound holds uniformly for all i with probability at least $1 - 2n^{-9}$. We now bound the norm of $v_k^{(rw)}$. Recall that $v_k^{(rw)}$ is D -normalized such that $(v_k^{(rw)})^T D v_k^{(rw)} / pn = 1$, hence

$$(A.10) \quad \frac{pn}{\max_i D_{ii}} \leq \|v_k^{(rw)}\|^2 \leq \frac{pn}{\min_i D_{ii}}.$$

By (A.6) and by a first order expansion of $1/(1+x)$, both the upper and lower bounds are $1 + \mathcal{O}\left(\epsilon_n + \epsilon_n^{-d/4} \sqrt{\log n/n}\right)$, hence by a first order expansion of $\sqrt{1+x}$, we have

$$(A.11) \quad \|v_k^{(rw)}\| = \sqrt{\|v_k^{(rw)}\|^2} = 1 + \mathcal{O}\left(\epsilon_n + \epsilon_n^{-d/4} \sqrt{\log n/n}\right).$$

Plugging this and (A.9) back into (A.8) yields

$$(A.12) \quad \left\| \frac{D^{1/2}}{\sqrt{pn}} v_k^{(rw)} - v_k^{(rw)} \right\| = \mathcal{O}\left(\epsilon_n + \epsilon_n^{-d/4} \sqrt{\log n/n}\right).$$

Finally, substituting (A.4) and (A.12) into (A.3) and applying the union bound for the event that one of the bounds fails, we obtain that the following bound holds with probability at least $1 - 4K^2 n^{-10} - (4K + 8)n^{-9}$,

$$(A.13) \quad \|v_k - \alpha \phi_k(X)\| = \mathcal{O}\left(\epsilon_n + \epsilon_n^{-d/4-1/2} \sqrt{\log n/n}\right) \quad \forall k \leq K. \quad \blacksquare$$

A.2. Rate of convergence for α in theorems 4.1 and 4.2.

Lemma A.1. *Let u, ϕ be two vectors in \mathbb{R}^n such that:*

(i) $\|u\| = 1$

(ii) $\|\phi\| = 1 + \mathcal{O}(1/\sqrt{n})$

(iii) $\|u - \alpha \phi\| = \mathcal{O}(\epsilon_n + \epsilon_n^{-d/4-1/2} \sqrt{\log n/n})$ for $\epsilon_n = o(1)$

Then it follows that

$$(A.14) \quad |\alpha| = 1 + \mathcal{O}(\epsilon_n + \epsilon_n^{-d/4-1/2} \sqrt{\log n/n}).$$

Proof. By the inverse triangle inequality, and (iii) we have

$$(A.15) \quad \left| \|u\| - |\alpha| \|\phi\| \right| \leq \|u - \alpha \phi\| = \mathcal{O}(\epsilon_n + \epsilon_n^{-d/4-1/2} \sqrt{\log n/n})$$

From (i) and (ii), we have that

$$(A.16) \quad \left| \|u\| - |\alpha| \|\phi\| \right| = \left| 1 - |\alpha| (1 + \mathcal{O}(1/\sqrt{n})) \right|$$

By combining (A.15) and (A.16), we obtain

$$(A.17) \quad |\alpha| (1 + \mathcal{O}(1/\sqrt{n})) = 1 + \mathcal{O}(\epsilon_n + \epsilon_n^{-d/4-1/2} \sqrt{\log n/n}).$$

Since $1/(1+x) = 1 - x + \mathcal{O}(x^2)$, we have that $1/(1 + \mathcal{O}(1/\sqrt{n})) = 1 + \mathcal{O}(1/\sqrt{n})$. Dividing both sides by $1 + \mathcal{O}(1/\sqrt{n})$ we obtain

$$(A.18) \quad |\alpha| = \left(1 + \mathcal{O}(\epsilon_n + \epsilon_n^{-d/4-1/2} \sqrt{\log n/n})\right) (1 + \mathcal{O}(1/\sqrt{n}))$$

$$(A.19) \quad = 1 + \mathcal{O}(\epsilon_n + \epsilon_n^{-d/4-1/2} \sqrt{\log n/n}),$$

where the last equality follows from the fact that $1/\sqrt{n} = \mathcal{O}(\epsilon_n + \epsilon_n^{-d/4-1/2} \sqrt{\log n/n})$. \blacksquare

A.3. Auxiliary lemmas for the proof of lemma 4.3 and Theorem 4.4.

Lemma A.2. Let $v^A = u^A - \epsilon^A$ and $v^B = u^B - \epsilon^B$ be two vectors that satisfy:

1. $\|v^A\| = \|v^B\| = 1$.
2. The vector u^A is proportional to u^B such that $u^A = cu^B$ for some constant c .
3. The vectors norms $\|\epsilon^A\|, \|\epsilon^B\|$ are both $\mathcal{O}(\epsilon_n)$.

Then $|(v^A)^T v^B| = 1 - \mathcal{O}(\epsilon_n)$.

Proof. We begin by deriving a bound over $\|u^A\|$ and $\|u^B\|$ using the reverse triangle inequality,

$$(A.20) \quad \begin{aligned} \|v^A\| &= \|u^A - \epsilon^A\| \geq \|u^A\| - \|\epsilon^A\| \\ \|v^A\| &\geq \|u^A\| - \|\epsilon^A\|. \end{aligned}$$

Thus, combined with assumptions (1) and (3), we get,

$$(A.21) \quad \|u^A\| \geq 1 - \mathcal{O}(\epsilon_n).$$

A similar bound can be derived for $\|u^B\|$. Next, we show that $|(u^A)^T u^B| \geq 1 - \mathcal{O}(\epsilon_n)$. Since $u^A = cu^B$, then $\frac{|(u^A)^T u^B|}{\|u^A\| \|u^B\|} = 1$. Thus, combining (A.21) and the above, we get

$$(A.22) \quad |(u^A)^T u^B| = \|u^A\| \cdot \|u^B\| \geq 1 - \mathcal{O}(\epsilon_n).$$

Finally, we derive a bound for $|(v^A)^T v^B|$. By the reverse triangle inequality

$$(A.23) \quad |(v^A)^T v^B| = |(u^A - \epsilon^A)^T (u^B - \epsilon^B)|$$

$$(A.24) \quad \geq |(u^A)^T u^B| - |(\epsilon^A)^T u^B| - |(\epsilon^B)^T u^A| - |(\epsilon^A)^T \epsilon^B|.$$

We showed that the first term is lower bounded by $1 - \mathcal{O}(\epsilon_n)$. By the assumed bound on the norms of ϵ^A, ϵ^B , the fourth term is bounded also by $\mathcal{O}(\epsilon_n^2)$. The second and third terms can be bounded by Cauchy-Schwartz inequality as follows,

$$(A.25) \quad |(\epsilon^A)^T u^B| \leq \|\epsilon^A\| \|u^B\| = \mathcal{O}(\epsilon_n).$$

Therefore, we have shown that

$$(A.26) \quad |(v^A)^T v^B| \geq 1 - \mathcal{O}(\epsilon_n). \quad \blacksquare$$

Lemma A.3. Let $V, U \in \mathbb{R}^{n \times K}$ be orthogonal matrices with columns v_i and u_i such that

$$(A.27) \quad v_i^T u_i \geq 1 - \epsilon \quad \forall i = 1, \dots, K,$$

Then $\|V - U\|^2 \leq 2K\epsilon$.

Proof. If $v_i^T u_i \geq 1 - \epsilon$ then $\|v_i - u_i\|^2 = 2(1 - v_i^T u_i) \leq 2\epsilon$. The spectral norm of a matrix is bounded by its Frobenius norm. Thus,

$$(A.28) \quad \|V - U\|^2 \leq \|V - U\|_F^2 \leq 2K\epsilon. \quad \blacksquare$$

Lemma A.4. *Let $A \in \mathbb{R}^{n \times n}$ be a symmetric positive semi-definite matrix, with eigenvectors and eigenvalues u_ℓ, λ_ℓ . The spectral decomposition of A is given by $A = \sum_\ell \lambda_\ell u_\ell u_\ell^T$. Let $V \in \mathbb{R}^{n \times K}$ be a matrix whose columns $\{v_i\}_{i=1}^K$ are orthogonal. If $|v_i^T u_j| \leq \epsilon \leq 1/\sqrt{n}$ for all (i, j) then*

$$(A.29) \quad \|A - (I - VV^T)A(I - VV^T)\| \leq K\epsilon^2 \sum_\ell \lambda_\ell.$$

Proof. Since A is symmetric, the spectral norm of $A - (I - VV^T)A(I - VV^T)$ is equal to the largest eigenvalue, given by

$$(A.30) \quad \max_{\|z\|=1} |z^T (A - (I - VV^T)A(I - VV^T))z|.$$

The proof of our claim is given in three steps:

1. We prove that the maximizer z^* of Eq. (A.30) is a linear combination of the vectors in $\{v_i\}$ such that $z^* = \sum_{j=1}^K \alpha_j v_j$. This implies that for z^* ,

$$(A.31) \quad (z^*)^T (A - (I - VV^T)A(I - VV^T))z^* = (z^*)^T A z^*.$$

2. For every pair of vectors v_i, v_j we derive the bound

$$(A.32) \quad v_j^T A v_i \leq \epsilon^2 \sum_\ell \lambda_\ell$$

3. Combining (i) + (ii) we show that the maximizer is bounded by

$$(A.33) \quad z^* A z^* = \sum_{i,j} \alpha_i \alpha_j \epsilon^2 \sum_l \lambda_l.$$

Together with the bound $\sum_{i,j} |\alpha_i| |\alpha_j| \leq K$ this concludes the proof. We now prove the three steps. For step (i), any vector z orthogonal to V satisfies,

$$(A.34) \quad z^T (A - (I - VV^T)A(I - VV^T))z = z^T A z - z^T A z = 0$$

Thus, the matrix $(A - (I - VV^T)A(I - VV^T))$ has a zero eigenvalue with multiplicity $n - K$. Since it is a symmetric matrix, it exhibits a spectral decomposition of K eigenvectors with non-zero eigenvalues all in the span of $\{v_i\}_{i=1}^K$. This implies specifically that the leading eigenvector z^* is a linear combination of $\{v_i\}_{i=1}^K$. Thus, $VV^T z^* = z^*$, and hence

$$(A.35) \quad (z^*)^T (A - (I - VV^T)A(I - VV^T))z^* = (z^*)^T A z^*.$$

Step (ii) follows almost immediately from $|v_i^T u_j| \leq \epsilon$,

$$(A.36) \quad |v_j^T A v_i| = \left| v_j^T \sum_{\ell=1}^n \lambda_\ell u_\ell u_\ell^T v_i \right| \leq \sum_{\ell=1}^n \lambda_\ell |u_\ell^T v_j| |u_\ell^T v_i| \leq \epsilon^2 \sum_{\ell=1}^n \lambda_\ell.$$

For step (iii), Let $z^* = \sum_{i=1}^K \alpha_i v_i$. By Eq. (A.31), the maximal eigenvalue is bounded by

$$(A.37) \quad |z^* A z^*| = \left| \sum_{ij} \alpha_i \alpha_j v_i^T A v_j \right| \leq \sum_{ij} |\alpha_i \alpha_j v_i^T A v_j| \leq \sum_{\ell} \lambda_{\ell} \epsilon^2 \sum_{ij} |\alpha_i \alpha_j|.$$

Finally, we have that $\sum_{ij} |\alpha_i \alpha_j| = \left(\sum_i |\alpha_i| \right)^2$. The maximum value of $\sum_i |\alpha_i|$, under the unit norm constraint $\sum_i \alpha_i^2 = 1$ is attained for $\alpha_i = 1/\sqrt{K}$, which gives $\sum_{ij} |\alpha_i \alpha_j| = K$. ■

Lemma A.5. *Let M be a symmetric and positive semi-definite matrix. Let $V, U \in \mathbb{R}^{n \times K}$ be two orthogonal matrices such that $V^T V = U^T U = I$, and let $Q_1 = I - V V^T$ and $Q_2 = I - U U^T$ be two projection matrices. Then,*

$$(A.38) \quad \|Q_1 M Q_1 - Q_2 M Q_2\| \leq 4 \|M\| \|U - V\|.$$

Proof. Since M is symmetric, the spectral norm is equal to the largest eigenvalue, give by,

$$(A.39) \quad \max_{\|x\|=1} \left| x^T (Q_1 M Q_1 - Q_2 M Q_2) x \right|.$$

As M is positive semi-definite, it has a square root, denoted $M^{0.5}$. Thus for any x we have

$$(A.40) \quad \begin{aligned} |x^T (Q_1 M Q_1 - Q_2 M Q_2) x| &= |x^T Q_1 M Q_1 x - x^T Q_2 M Q_2 x| \\ &= \left| \|M^{0.5} Q_1 x\|^2 - \|M^{0.5} Q_2 x\|^2 \right| \\ &= \left| \|M^{0.5} Q_1 x\| + \|M^{0.5} Q_2 x\| \right| \cdot \left| \|M^{0.5} Q_2 x\| - \|M^{0.5} Q_1 x\| \right|. \end{aligned}$$

By Cauchy-Shwartz we have $\|M^{0.5} Q_1 x\| \leq \|M^{0.5}\|$ and $\|M^{0.5} Q_2 x\| \leq \|M^{0.5}\|$. By the reverse triangle inequality,

$$(A.41) \quad \begin{aligned} \left| \|M^{0.5} Q_2 x\| - \|M^{0.5} Q_1 x\| \right| &\leq \|M^{0.5} (Q_1 - Q_2) x\| \\ &\leq \|M^{0.5}\| \|Q_1 - Q_2\| = \|M^{0.5}\| \|V_1 V_1^T - V_2 V_2^T\|. \end{aligned}$$

To bound the norm $\|V_1 V_1^T - V_2 V_2^T\|$ we apply again the reverse triangle inequality. For every vector x we have,

$$(A.42) \quad \begin{aligned} |x^T (V_1 V_1^T - V_2 V_2^T) x| &\leq \left| \|V_1^T x\|^2 - \|V_2^T x\|^2 \right| = (\|V_1^T x\| + \|V_2^T x\|) (\|V_1^T x\| - \|V_2^T x\|). \\ &\leq 2 \| (V_1 - V_2)^T x \| \leq 2 \|V_1 - V_2\|. \end{aligned}$$

Combining the bounds in Eqs. (A.42), (A.41) and (A.40) yields

$$(A.43) \quad \|Q_1 M Q_1 - Q_2 M Q_2\| \leq 4 \|M\| \|V_1 - V_2\|. \quad \blacksquare$$

A.4. Proof of Lemma 4.3. By Theorem 4.2, with probability $> 1 - 4K^2n^{-10} - (4K+8)n^{-9}$ there exists a constant α^A such that the unit-normalized eigenvector $v_{l,k}^A$ satisfies

$$(A.44) \quad \left\| \frac{\alpha^A}{\sqrt{np^A}} \rho_X(f_{l,k}^A) - v_{l,k}^A \right\|_2 = \mathcal{O} \left(\epsilon_n + \epsilon_n^{-d/4-1/2} \sqrt{\log n/n} \right),$$

for all eigenfunctions $f_{l,k}^A$ that correspond to eigenvalues $\eta_{l,k}^A$ that are among the smallest K eigenvalues of the Laplace-Beltrami operator on \mathcal{M}^A . The same result holds for α^B , $f_{m,k'}^B$, $\eta_{m,k'}^B$ and $v_{m,k'}^B$. We denote by $\epsilon_{l,k}^A$ the difference $\frac{\alpha^A}{\sqrt{np^A}} \rho_X(f_{l,k}^A) - v_{l,k}^A$ and bound the inner product of $v_{l,k}^A$ and $v_{m,k'}^B$ using the triangle inequality,

$$(A.45) \quad \begin{aligned} |(v_{l,k}^A)^T v_{m,k'}^B| &= \left| \left(\frac{\alpha^A}{\sqrt{np^A}} \rho_X(f_{l,k}^A) - \epsilon_{l,k}^A \right)^T \left(\frac{\alpha^B}{\sqrt{np^B}} \rho_X(f_{m,k'}^B) - \epsilon_{m,k'}^B \right) \right| \\ &\leq \frac{\alpha^A \alpha^B}{n \sqrt{p^A p^B}} |\rho_X(f_{l,k}^A)^T \rho_X(f_{m,k'}^B)| \\ &\quad + \frac{\alpha^B}{\sqrt{np^B}} |(\epsilon_{l,k}^A)^T \rho_X(f_{m,k'}^B)| + \frac{\alpha^A}{\sqrt{np^A}} |(\rho_X(f_{l,k}^A))^T \epsilon_{m,k'}^B| + |(\epsilon_{l,k}^A)^T \epsilon_{m,k'}^B|. \end{aligned}$$

The second and third terms in Eq. (A.45) can be bounded via the Cauchy-Schwartz inequality. For example, the second term is bounded by

$$(A.46) \quad \frac{\alpha^B}{\sqrt{np^B}} |(\epsilon_{l,k}^A)^T \rho_X(f_{m,k'}^B)| \leq \frac{\alpha^B}{\sqrt{np^B}} \|\epsilon_{l,k}^A\| \|\rho_X(f_{m,k'}^B)\|.$$

Lemma 3.4 in [7], w.p. $> 1 - 2K^2n^{-10}$, the term $\frac{1}{np^B} \|\rho_X(f_{m,k'}^B)\|^2$ is $1 + \mathcal{O}_p(\log(n)/n)$. This result together with the bound on $\|\epsilon_{l,k}^A\|$, $\|\epsilon_{m,k'}^B\|$ in Theorem 4.2, and the concentration of α^B by Lemma A.1 yields,

$$(A.47) \quad \frac{\alpha^B}{\sqrt{np^B}} |(\epsilon_{l,k}^A)^T \rho_X(f_{m,k'}^B)| + \frac{\alpha^A}{\sqrt{np^A}} |(\epsilon_{m,k'}^B)^T \rho_X(f_{l,k}^A)| = \mathcal{O} \left(\epsilon_n + \sqrt{\frac{\log n}{n \epsilon_n^{d/2+1}}} \right).$$

The fourth term is negligible,

$$(A.48) \quad |(\epsilon_{m,k'}^B)^T \epsilon_{l,k}^A| \leq \|(\epsilon_{m,k'}^B)\| \|\epsilon_{l,k}^A\| = \mathcal{O} \left(\left(\epsilon_n + \sqrt{\frac{\log n}{n \epsilon_n^{d/2+1}}} \right)^2 \right)$$

The first term of Eq. (A.45) is equal to,

$$(A.49) \quad \begin{aligned} \frac{\alpha^A \alpha^B}{n \sqrt{p^A p^B}} |\rho_X(f_{l,k}^A)^T \rho_X(f_{m,k'}^B)| &= \frac{\alpha^A \alpha^B}{n \sqrt{p^A p^B}} \left| (\rho_{\pi_1(X)}(f_l^{(1)}) \cdot \rho_{\pi_3(X)}(f_k^{(3)}))^T (\rho_{\pi_2(X)}(f_m^{(2)}) \cdot \rho_{\pi_3(X)}(f_{k'}^{(3)})) \right| \\ &= \frac{\alpha^A \alpha^B}{n \sqrt{p^A p^B}} \left| \sum_{i=1}^n f_l^{(1)}(\pi_1(x_i)) f_m^{(2)}(\pi_2(x_i)) f_k^{(3)}(\pi_3(x_i)) f_{k'}^{(3)}(\pi_3(x_i)) \right|. \end{aligned}$$

Consider the summands in Eq. (A.49). In our model, the coordinates on different manifolds are independently drawn. Thus, taking the expectation of the summands gives,

$$(A.50) \quad \begin{aligned} & \mathbb{E}[f_l^{(1)}(\pi_1(x))f_m^{(2)}(\pi_2(x))f_k^{(3)}(\pi_3(x))f_{k'}^{(3)}(\pi_3(x))] \\ &= \mathbb{E}[f_l^{(1)}(\pi_1(x))]\mathbb{E}[f_m^{(2)}(\pi_2(x))]\mathbb{E}[f_k^{(3)}(\pi_3(x))f_{k'}^{(3)}(\pi_3(x))]. \end{aligned}$$

In addition, by the orthogonality of eigenfunctions with different eigenvalues, we have,

$$(A.51) \quad \begin{aligned} \mathbb{E}[f_l^{(1)}(\pi_1(x))] &= 0 \quad \forall l > 0, \\ \mathbb{E}[f_m^{(2)}(\pi_2(x))] &= 0 \quad \forall m > 0, \\ \mathbb{E}[f_k^{(3)}(\pi_3(x))f_{k'}^{(3)}(\pi_3(x))] &= 0 \quad \forall (k \neq k'). \end{aligned}$$

As for the second moment, we have

$$(A.52) \quad \begin{aligned} \mathbb{E}[(f_l^{(1)}(\pi_1(x)))^2] &= 1 \quad \forall l, \\ \mathbb{E}[(f_m^{(2)}(\pi_2(x)))^2] &= 1 \quad \forall m, \\ \mathbb{E} \left[\left(f_k^{(3)}(\pi_3(x))f_{k'}^{(3)}(\pi_3(x)) \right)^2 \right] &\leq 1 \quad \forall (k, k'). \end{aligned}$$

Eqs. (A.50), (A.51) and (A.52) imply that unless $l = m = 0$ and $k = k'$, the sum in Eq. (A.49) is over centred i.i.d random variables with variance ≤ 1 . Since the terms are i.i.d. the variance of the sum is the sum of variances and is thus bounded by n . Therefore,

$$(A.53) \quad \frac{\alpha^A \alpha^B}{n\sqrt{p_A p_B}} \left| \rho_X(f_{l,k}^A)^T \rho_X(f_{m,k'}^B) \right| = \frac{\alpha^A \alpha^B}{\sqrt{p_A p_B}} \mathcal{O}_p(1/\sqrt{n}) = \mathcal{O}_p(1/\sqrt{n}).$$

It is easy to see that if $\epsilon_n < 1$ then $1/\sqrt{n} < \epsilon_n^{-d/4-1/2} \sqrt{\log n/n}$ and if $\epsilon_n \geq 1$ then $1/\sqrt{n} < \epsilon_n$. In both cases, $1/\sqrt{n}$ is negligible with respect to the other terms (Eqs. (A.47) and (A.48)). Thus for $k \neq k'$, we have

$$(A.54) \quad (v_{l,k}^A)^T v_{m,k'}^B = \mathcal{O} \left(\epsilon_n + \sqrt{\frac{\log n}{n\epsilon_n^{d/2+1}}} \right).$$

The only remaining case is when $l = m = 0$ and $k = k'$. Since $f_0^{(1)}, f_0^{(2)}$ are both constant functions, then by Eq. (4.8) we have

$$(A.55) \quad \rho_X(f_{0,k}^A) \sim \rho_{\pi_1(X)}(f_0^{(1)}) \rho_{\pi_3(X)}(f_k^{(3)}) \sim \rho_{\pi_3(X)} f_k^{(3)}.$$

A similar derivation can be done for $\rho_X(f_{0,k'}^B)$ which implies that $\rho_X(f_{0,k}^A) \sim \rho_X(f_{0,k'}^B)$. Let $u^A = \frac{\alpha^A}{\sqrt{np_A}} \rho_X(f_{0,k}^A)$ and $u^B = \frac{\alpha^B}{\sqrt{np_B}} \rho_X(f_{0,k}^B)$. We invoke Lemma A.2 with u^A, u^B and $\epsilon_{0,k}^A, \epsilon_{0,k}^B$ to obtain that

$$(A.56) \quad |(v_{0,k}^A)^T v_{0,k}^B| = 1 - \mathcal{O}(\|\epsilon_{0,k}^A\| + \|\epsilon_{0,k}^B\|).$$

This result together with the bounds on $\|\epsilon_{0,k}^A\|, \|\epsilon_{0,k}^B\|$ from Theorem 4.2 concludes the proof. ■

A.5. Proof of Theorem 4.4.

Step 1: Recall that V^{B_θ} contains the eigenvectors of P_τ^B , associated with the shared variables. Thus, the matrix $E_1 = Q^{B_\theta} P_\tau^B Q^{B_\theta}$ contains the symmetric projection of P_τ^B onto the orthogonal complement of its leading eigenvectors $\{v_{0,1}^B, v_{0,2}^B, \dots, v_{0,K}^B\}$, which eliminates those eigenvectors. Due to the eigenvalue structure of the product manifold \mathcal{M}_B (see Eq. (4.9)) it follows that for a large enough K , the leading eigenvector of E_1 is thus $v_{1,0}^B$, which is the leading eigenvector that is *not* associated with θ .

$$(A.57) \quad \arg \max_{\|v\|=1} v^T E_1 v = v_{1,0}^B.$$

By Theorem. 4.2 we obtain that as $n \rightarrow \infty$,

$$(A.58) \quad \left\| v_{1,0}^B - \frac{\alpha}{\sqrt{pn}} \rho_X(f_{1,0}^B) \right\| = \mathcal{O} \left(\epsilon_n + \sqrt{\frac{\log n}{n\epsilon_n^{d/2+1}}} \right).$$

Step 2: To bound the spectral norm $\|E_2 - E_1\|$, we add and subtract $Q^{A_\psi} Q^{B_\theta} P_\tau^B Q^{B_\theta} Q^{A_\psi}$ and then apply the triangle inequality,

$$(A.59) \quad \begin{aligned} \|Q^{A_\psi} Q^{A_\theta} P_\tau^B Q^{A_\theta} Q^{A_\psi} - Q^{B_\theta} P_\tau^B Q^{B_\theta}\| &\leq \underbrace{\|Q^{A_\psi} Q^{A_\theta} P_\tau^B Q^{A_\theta} Q^{A_\psi} - Q^{A_\psi} Q^{B_\theta} P_\tau^B Q^{B_\theta} Q^{A_\psi}\|}_{\text{I}} \\ &+ \underbrace{\|Q^{A_\psi} Q^{B_\theta} P_\tau^B Q^{B_\theta} Q^{A_\psi} - Q^{B_\theta} P_\tau^B Q^{B_\theta}\|}_{\text{II}} \end{aligned}$$

We begin by bounding I,

$$\begin{aligned} \|Q^{A_\psi} Q^{A_\theta} P_\tau^B Q^{A_\theta} Q^{A_\psi} - Q^{A_\psi} Q^{B_\theta} P_\tau^B Q^{B_\theta} Q^{A_\psi}\| &= \|Q^{A_\psi} (Q^{A_\theta} P_\tau^B Q^{A_\theta} - Q^{B_\theta} P_\tau^B Q^{B_\theta}) Q^{A_\psi}\| \\ &\leq \|Q^{A_\theta} P_\tau^B Q^{A_\theta} - Q^{B_\theta} P_\tau^B Q^{B_\theta}\| \leq 4 \|P_\tau^B\| \|V^{A_\theta} - V^{B_\theta}\| \end{aligned}$$

The first inequality follows from the inequality $\|AB\| \leq \|A\| \|B\|$ that holds for all operator norms, and since Q^{A_ψ} is a projection matrix, we have $\|Q^{A_\psi}\| \leq 1$. The second inequality is proved in Lemma A.5. Combining lemma 4.3 with Lemma A.3 gives

$$(A.60) \quad \|V^{B_\theta} - V^{A_\theta}\|^2 = \mathcal{O}_p \left(K \epsilon_n + K \sqrt{\frac{\log n}{n\epsilon_n^{d/2+1}}} \right).$$

This, combined with the bound on the eigenvalues of the operator, $\|P^B\| \leq 1$, yields the following inequality:

$$(A.61) \quad \|Q^{A_\psi} Q^{A_\theta} P_\tau^B Q^{A_\theta} Q^{A_\psi} - Q^{A_\psi} Q^{B_\theta} P_\tau^B Q^{B_\theta} Q^{A_\psi}\|^2 \leq \mathcal{O}(K \epsilon_n) + \mathcal{O} \left(K \sqrt{\frac{\log n}{n\epsilon_n^{d/2+1}}} \right).$$

Next, we bound term II of Eq. (A.59). We apply Lemma A.4 with the matrix $Q^{B_\theta} P_\tau^B Q^{B_\theta}$ and projection Q^{A_ψ} . The bound ϵ on the inner products between a vector in the span of Q^{B_θ}

and the eigenvectors of P_τ^B , as required in the Lemma is given by Lemma 4.3. This yields

$$\begin{aligned} \|Q^{A_\psi} Q^{B_\theta} P_\tau^B Q^{B_\theta} Q^{A_\psi} - Q^{B_\theta} P_\tau^B Q^{B_\theta}\| &= \left(\sum_{l,k: \lambda_{l,k}^A < \tau} (1 - \lambda_{l,k}^A) \right) \mathcal{O} \left(K\epsilon_n + K \sqrt{\frac{\log n}{n\epsilon_n^{d/2+1}}} \right) \\ (A.62) \qquad \qquad \qquad &= \mathcal{O}(K^2\epsilon_n) + \left(K^2 \sqrt{\frac{\log n}{n\epsilon_n^{d/2+1}}} \right). \end{aligned}$$

The convergence in Eq. (A.61) is slower than Eq. (A.62). Thus, the overall convergence rate of $\|E_2 - E_1\|^2$ is,

$$(A.63) \qquad \qquad \qquad \|E_2 - E_1\|^2 = \mathcal{O}(K\epsilon_n) + \mathcal{O} \left(K \sqrt{\frac{\log n}{n\epsilon_n^{d/2+1}}} \right).$$

Step 3: We apply the Davis-Kahan Theorem to the symmetric matrices E_1 and E_2 and their respective leading eigenvectors δ^B and $v_{1,0}^B$. According to the theorem, given that $(\delta^B)^T v_{1,0}^B \geq 0$, the following inequality holds [48, Corollary 1]:

$$(A.64) \qquad \qquad \qquad \|\delta^B - v_{1,0}^B\|^2 \leq \frac{2^{\frac{4}{3}} \|E_2 - E_1\|^2}{\gamma_K^2}$$

where γ_K is the minimal spectral gap, which under assumption (ii) is larger than zero. Combining the outcome of step 2 (Eq. (A.63)) with the Davis-Kahan theorem yields,

$$(A.65) \qquad \qquad \qquad \|\delta^B - v_{1,0}^B\|^2 \leq \mathcal{O}(K\epsilon_n) + \mathcal{O} \left(K \sqrt{\frac{\log n}{n\epsilon_n^{d/2+1}}} \right)$$

Finally, the outcome of step 1 (Eq. (A.58)) and step 3 (Eq. (A.65)) completes the proof.

$$(A.66) \qquad \qquad \qquad \left\| \delta^B - \frac{\alpha}{p\sqrt{n}} \rho_{\pi_2(x)}(f_1^{(2)}) \right\|^2 = \mathcal{O}(\|\delta^B - v_{1,0}^B\|^2) + \mathcal{O} \left(\left\| v_{1,0}^B - \alpha \frac{1}{\sqrt{pn}} \rho_X(f_{1,0}) \right\|^2 \right)$$

$$(A.67) \qquad \qquad \qquad \leq \mathcal{O} \left(K\epsilon_n + K \sqrt{\frac{\log n}{n\epsilon_n^{d/2+1}}} \right).$$

■

References.

- [1] E. ABBE, *Community detection and stochastic block models: recent developments*, Journal of Machine Learning Research, 18 (2018), pp. 1–86.
- [2] S. AKAHO, *A kernel method for canonical correlation analysis*, in International Meeting of Psychometric Society, 2001, vol. 1, 2001.
- [3] T. BENDORY, A. BARTESAGHI, AND A. SINGER, *Single-particle cryo-electron microscopy: Mathematical theory, computational challenges, and opportunities*, IEEE Signal Processing Magazine, 37 (2020), pp. 58–76.
- [4] J. CALDER AND N. G. TRILLOS, *Improved spectral convergence rates for graph laplacians on ε -graphs and k -nn graphs*, Applied and Computational Harmonic Analysis, 60 (2022), pp. 123–175.
- [5] K. CHAUDHURI, S. M. KAKADE, K. LIVESCU, AND K. SRIDHARAN, *Multi-view clustering via canonical correlation analysis*, in Proceedings of the 26th annual international conference on machine learning, 2009, pp. 129–136.
- [6] X. CHENG AND H.-T. WU, *Convergence of graph laplacian with knn self-tuned kernels*, Information and Inference: A Journal of the IMA, 11 (2021), p. 889–957.
- [7] X. CHENG AND N. WU, *Eigen-convergence of gaussian kernelized graph laplacian by manifold heat interpolation*, Applied and Computational Harmonic Analysis, 61 (2022), pp. 132–190.
- [8] D. COHEN, T. SHNITZER, Y. KLUGER, AND R. TALMON, *Few-sample feature selection via feature manifold learning*, in Proceedings of the 40th International Conference on Machine Learning, vol. 202, PMLR, 23–29 Jul 2023, pp. 6296–6319.
- [9] R. R. COIFMAN, N. F. MARSHALL, AND S. STEINERBERGER, *A common variable minimax theorem for graphs*, Foundations of Computational Mathematics, 23 (2023), pp. 493–517.
- [10] T. DIETHE, D. R. HARDOON, AND J. SHAWE-TAYLOR, *Multiview fisher discriminant analysis*, in NIPS workshop on learning from multiple sources, vol. 1, 2008.
- [11] D. B. DUNSON, H.-T. WU, AND N. WU, *Spectral convergence of graph Laplacian and heat kernel reconstruction in l^∞ from random samples*, Applied and Computational Harmonic Analysis, 55 (2021), pp. 282–336.
- [12] D. EYNARD, A. KOVNATSKY, M. M. BRONSTEIN, K. GLASHOFF, AND A. M. BRONSTEIN, *Multimodal manifold analysis by simultaneous diagonalization of laplacians*, IEEE transactions on pattern analysis and machine intelligence, 37 (2015), pp. 2505–2517.
- [13] R. A. FISHER, *The use of multiple measurements in taxonomic problems*, Annals of eugenics, 7 (1936), pp. 179–188.
- [14] K. FUKUNAGA AND W. L. KOONTZ, *Application of the Karhunen-Loeve expansion to feature selection and ordering*, IEEE Transactions on computers, 100 (1970), pp. 311–318.
- [15] N. GARCÍA TRILLOS, M. GERLACH, M. HEIN, AND D. SLEPČEV, *Error estimates for spectral convergence of the graph laplacian on random geometric graphs toward the Laplace-Beltrami operator*, Foundations of Computational Mathematics, 20 (2020), pp. 827–887.
- [16] J. HE, T. BRUGÈRE, AND G. MISHNE, *Product manifold learning with independent coordinate selection*, in Proceedings of 2nd Annual Workshop on Topology, Algebra, and Geometry in Machine Learning (TAG-ML), vol. 221, PMLR, 2023, pp. 267–277.

- [17] R. A. HORN AND C. R. JOHNSON, *Matrix analysis*, Cambridge university press, 2012.
- [18] H. HOTELLING, *Relations between two sets of variates*, Breakthroughs in statistics: methodology and distribution, (1992), pp. 162–190.
- [19] O. KATZ, R. R. LEDERMAN, AND R. TALMON, *Spectral flow on the manifold of spd matrices for multimodal data processing*, arXiv preprint arXiv:2009.08062, (2020).
- [20] J. KILEEL, A. MOSCOVICH, N. ZELESKO, AND A. SINGER, *Manifold learning with arbitrary norms*, Journal of Fourier Analysis and Applications, 27 (2021).
- [21] P. L. LAI AND C. FYFE, *Kernel and nonlinear canonical correlation analysis*, International journal of neural systems, 10 (2000), pp. 365–377.
- [22] R. R. LEDERMAN AND R. TALMON, *Learning the geometry of common latent variables using alternating-diffusion*, Applied and Computational Harmonic Analysis, 44 (2018), pp. 509–536.
- [23] C.-S. LEE, A. ELGAMMAL, AND M. TORIKI, *Learning representations from multiple manifolds*, Pattern Recognition, 50 (2016), pp. 74–87.
- [24] Y.-H. LI AND M. SAVVIDES, *Kernel fukunaga-koontz transform subspaces for enhanced face recognition*, in 2007 IEEE conference on computer vision and pattern recognition, IEEE, 2007, pp. 1–8.
- [25] O. LINDENBAUM, A. YEREDOR, M. SALHOV, AND A. AVERBUCH, *Multi-view diffusion maps*, Information Fusion, 55 (2020), pp. 127–149.
- [26] S. MAJI, H. LIAO, A. DASHTI, G. MASHAYEKHI, A. OURMAZD, AND J. FRANK, *Propagation of conformational coordinates across angular space in mapping the continuum of states from cryo-EM data by manifold embedding*, Journal of Chemical Information and Modeling, 60 (2020), p. 2484–2491.
- [27] B. MOHAR, Y. ALAVI, G. CHARTRAND, AND O. OELLERMANN, *The laplacian spectrum of graphs*, Graph theory, combinatorics, and applications, 2 (1991), p. 12.
- [28] A. MOSCOVICH, A. HALEVI, J. ANDÉN, AND A. SINGER, *Cryo-EM reconstruction of continuous heterogeneity by laplacian spectral volumes*, Inverse Problems, 36 (2020), p. 024003.
- [29] L. MOSES AND L. PACTHER, *Museum of spatial transcriptomics*, Nature Methods, 19 (2022), pp. 534–546.
- [30] B. RICAUD, P. BORGNAT, N. TREMBLAY, P. GONÇALVES, AND P. VANDERGHEYNST, *Fourier could be a data scientist: From graph fourier transform to signal processing on graphs*, Comptes Rendus Physique, 20 (2019), pp. 474–488.
- [31] A. SHARMA, K. K. PALIWAL, S. IMOTO, AND S. MIYANO, *A feature selection method using improved regularized linear discriminant analysis*, Machine vision and applications, 25 (2014), pp. 775–786.
- [32] Y. SHI, B. PAIGE, P. TORR, ET AL., *Variational mixture-of-experts autoencoders for multi-modal deep generative models*, Advances in neural information processing systems, 32 (2019).
- [33] T. SHNITZER, M. BEN-CHEN, L. GUIBAS, R. TALMON, AND H.-T. WU, *Recovering hidden components in multimodal data with composite diffusion operators*, SIAM Journal on Mathematics of Data Science, 1 (2019), pp. 588–616.
- [34] D. I. SHUMAN, S. K. NARANG, P. FROSSARD, A. ORTEGA, AND P. VANDERGHEYNST, *The emerging field of signal processing on graphs: Extending high-dimensional data analy-*

- sis to networks and other irregular domains*, IEEE signal processing magazine, 30 (2013), pp. 83–98.
- [35] N. SILBERMAN, D. HOIEM, P. KOHLI, AND R. FERGUS, *Indoor segmentation and support inference from rgbd images*, in Computer Vision–ECCV 2012: 12th European Conference on Computer Vision, Florence, Italy, October 7–13, 2012, Proceedings, Part V 12, Springer, 2012, pp. 746–760.
- [36] A. SINGER AND H.-T. WU, *Spectral convergence of the connection laplacian from random samples*, Information and Inference: A Journal of the IMA, 6 (2017), pp. 58–123.
- [37] F. SONG, D. MEI, AND H. LI, *Feature selection based on linear discriminant analysis*, in 2010 international conference on intelligent system design and engineering application, vol. 1, IEEE, 2010, pp. 746–749.
- [38] H. SPECHT, E. EMMOTT, A. A. PETELSKI, R. G. HUFFMAN, D. H. PERLMAN, M. SERRA, P. KHARCHENKO, A. KOLLER, AND N. SLAVOV, *Single-cell proteomic and transcriptomic analysis of macrophage heterogeneity using scope2*, Genome biology, 22 (2021), pp. 1–27.
- [39] R. D. SRISTI, G. MISHNE, AND A. JAFFE, *Disc: Differential spectral clustering of features*, Advances in Neural Information Processing Systems, 35 (2022), pp. 26269–26282.
- [40] M. TAHMASIAN, J. SHAO, C. MENG, T. GRIMMER, J. DIEHL-SCHMID, B. H. YOUSEFI, S. FÖRSTER, V. RIEDL, A. DRZEZGA, AND C. SORG, *Based on the network degeneration hypothesis: separating individual patients with different neurodegenerative syndromes in a preliminary hybrid pet/mr study*, Journal of Nuclear Medicine, 57 (2016), pp. 410–415.
- [41] B. TOADER, F. J. SIGWORTH, AND R. R. LEDERMAN, *Methods for cryo-em single particle reconstruction of macromolecules having continuous heterogeneity*, Journal of Molecular Biology, 435 (2023), p. 168020. New Frontier of Cryo-Electron Microscopy Technology.
- [42] U. VON LUXBURG, *A tutorial on spectral clustering*, Statistics and computing, 17 (2007), pp. 395–416.
- [43] U. VON LUXBURG, M. BELKIN, AND O. BOUSQUET, *Consistency of spectral clustering*, The Annals of Statistics, (2008), pp. 555–586.
- [44] C. WAH, S. BRANSON, P. WELINDER, P. PERONA, AND S. BELONGIE, *The caltech-ucsd birds-200-2011 dataset*, (2011).
- [45] C. L. WORMELL AND S. REICH, *Spectral convergence of diffusion maps: Improved error bounds and an alternative normalization*, SIAM Journal on Numerical Analysis, 59 (2021), pp. 1687–1734.
- [46] C. XU, D. TAO, AND C. XU, *A survey on multi-view learning*, arXiv preprint arXiv:1304.5634, (2013).
- [47] O. YAIR AND R. TALMON, *Local canonical correlation analysis for nonlinear common variables discovery*, IEEE Transactions on Signal Processing, 65 (2016), pp. 1101–1115.
- [48] Y. YU, T. WANG, AND R. J. SAMWORTH, *A useful variant of the davis–kahan theorem for statisticians*, Biometrika, 102 (2015), pp. 315–323.
- [49] L. ZELNIK-MANOR AND P. PERONA, *Self-tuning spectral clustering*, Advances in neural information processing systems, 17 (2004).
- [50] S. ZHANG, A. MOSCOVICH, AND A. SINGER, *Product manifold learning*, in International

- Conference on Artificial Intelligence and Statistics, PMLR, 2021, pp. 3241–3249.
- [51] Y. ZHAO, X. YOU, S. YU, C. XU, W. YUAN, X.-Y. JING, T. ZHANG, AND D. TAO, *Multi-view manifold learning with locality alignment*, Pattern Recognition, 78 (2018), pp. 154–166.
- [52] E. D. ZHONG, T. BEPLER, B. BERGER, AND J. H. DAVIS, *CryoDRGN: reconstruction of heterogeneous cryo-EM structures using neural networks*, Nature Methods, 18 (2021), p. 176–185.